CONTROL, OPTIMIZATION AND TOMOGRAPHY OF SUPERCONDUCTING QUBITS

The Hebrew University of Jerusalem

Faculty of Science

Racah Institute of Physics

By

Roy Resh

Student number: 039594627

Supervisor: Dr. Nadav Katz

Thesis submitted for the degree of Master of Science

January 2013

Acknowledgements

This work could not have been done without the help and contribution of several people. First of all, I would like to thank my supervisor, Dr. Nadav Katz, for his extraordinary guidance. In the begininning of this work, Nadav has emphasized the difference between being a student and a reseacher where instead of solving well-defined problems, one has to ask questions and try to find solutions. This has encouraged me to think more deeply about each problem. Discussions with Nadav have always been fruitful and he can always point at the heart of each experimental challenge or theoretical question. I would like to thank Yoni Shalibo, who has lead a large part of this research, whom with I have enjoyed working. This work involves a complex experimental set-up and Yoni has always answered my frequent questions with patience. I would like to thank my lab partners: David Shwa, Ofer Fogel and Raffi Cohen for their help in my research and for their pleasent company. I wish to thank Prof. Yuval Gefen, Dr. Alessandro Romito and Oded Zilberberg for fertile discussions that have led to the development of the state discrimination protocol in the Josephson phase qubit. Finally, I thank my fiancee Moran Raveh who supported me all along and my parents for their endless love.

Abstract

Quantum computing is a relatively new area of research, both theoretically and experimentally. A quantum computer is made of quantum bits (qubits), two-level quantum systems that can be controlled and entangled at will, and thus can perform algorithms. In reality, these quantum systems can be manifested using a variety of physical systems: photons, nitrogen-vacancy centres in diamonds, cold ions, superconducting ciruits and several other systems. A majority of these systems consist of multiple energy levels in which only the bottom two levels are used. The ability to control and measure the higher excited levels can be used as an additional computing resource for optimizing gates by reducing the number of qubit operations or alternatively by reducing the number of qubits. However, control and measurement of these levels pose a challenge.

In this work we present new methods of control and measurement of multi-level states in a superconducting Josephson phase qubit. Section 3.1 presents a genetic optimization method of preparing multi-level states in the phase qubit. Section 3.2 describes phase space measurement in the phase qubit and its application as an efficient multi-level state tomography technique. Moreover, it is used to directly observe phase locking between the system and the drive in states prepared by a frequency-chirp. Chapter 4 details theoretical simulations that were done to analyze the feasibility of two future experiments in superconducting qubits. The first one is a state discrimination technique for discerning between a slighlty excited state and a pure ground state with high fidelity which can be incorporated into future experimental sequences in which a high degree of purity is needed. The second simulation was done to determine the possibility of an experimental confirmation of a theory of the dynamics of a

four-level system using group theory. The theoretical understanding of multi-level dynamics is important for the implementations of multi-level quantum logic. Both experiments were found to be acheivable in currently available samples.

Another part of this work was to set-up an experimental system that can measure the transmon qubit. This qubit features higher coherence times in comparison with the phase qubit and is measured by a different method. In addition, a transmon sample was measured but unfortunately was found to be unusable. Finally, the appendices provide information on simulation methods and calibration techniques of the electronics used in the experiment. Proper calibration of the control electronics is crucial to acheive the results presented in this work.

Contents

1 General Introduction

CHAPTER 1

General Introduction

1.1 Multi-Level Excitations in Quantum Systems

1.1.1 Motivation

Quantum computation is a growing field of research in the past 20 years. Its goal is to construct a quantum computer comprising of a large number of entangled quantum bits (qubits) which can be coherently controlled in order to perform gate operations for quantum algorithms[1]. A famous quantum algorithm is Shor's factoring algorithm that can decipher RSA code exponentially faster than classical computers. From a scientific point of view, a quantum computer can serve as a universal quantum simulator that can be programmed to simulate any local quantum system [2]. Quantum bits are realized by any two-level quantum system. This is typically done by the resonant excitation of a specific transition on systems that are naturally far more complex and have many accessible degrees of freedom such as atoms, ions or photons.

There are many obstacles in the realization of a quantum computer that will require both theoretical and technological developments to overcome. One of them is the difficulty of controlling and entangling a large number of qubits. It has been suggested that by harnessing the higher levels of a quantum system it is possible to reduce the number of qubits for various operations by a factor of $\log_2 d$ where d is the number of levels in the multi-level quantum system (qudit)[3]. Lanyon et al[4] have shown that the $n-$control-qubit Toffoli gate and the n-control-qubit unitary gate can be performed with a smaller number of two-qubit gates or alternatively a smaller number of ancilla qubits using a three level bit (qutrit), thus reducing the physical resources for the computation protocol. Multilevel qubits can naturally simulate physical systems with spin greater than $1/2$ [5] and show stronger violations of local realism when prepared in entangled states [6]. Quantum error correction codes have been extended to multiple qudits [7], paving the way for efficient multi-level quantum computing.

1.1.2 Experimental Realization

While the manipulation of a two-level qubit has been shown in all of these systems, control of a multi-level system has been demonstrated in a smaller number of systems. Multilevel systems have been successfully realized in photon orbital angular momentum states[8, 9], polarization states of multiple photons[10] and energy-time entangled qutrits[11]. In the area of superconductivity, qutrit tomography was demonstrated in the transmon qubit[12]. This work focuses on superconducting electrical circuits that can serve as a quantum bit. One of its advantages is its scalability: the ability to fabricate a system of multiple entangled qubits. The ability to coherently control multilevel states in a superconducting qubit is demonstrated which can be used as a physical realization of the protocols described in the previous section.

1.2 Coherent Dynamics of Two-Level System

Coherent dynamics of a quantum two-level system is fundamental to the understanding of quantum systems. It is important because it is very general:

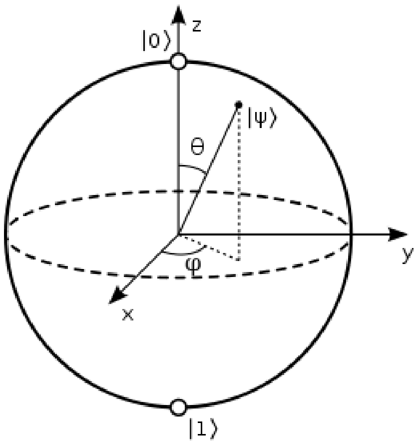

Fig. 1.1: Bloch sphere desciption of a two-level quantum system. The state is described by two angles θ and φ representing the state $|\Psi\rangle = \cos(\theta/2)\,|0\rangle + \sin(\theta/2)\,e^{i\varphi}|1\rangle$. The poles indicate the two eigenstates $|0\rangle$ and $|1\rangle$.

every system in which coherent resonant interactions involve only two of its energy levels can be described by the formalism stated in this section. The basic effects in the coherent manipulation of a quantum bit in every physical system are governed by the equations describing the dynamics of a two-level system named the *Bloch* equations.

Consider a quantum two-level system represented by the states $|0\rangle$ and $|1\rangle$ with an unperturbed Hamiltonian $\hat{H}_0$ such that:

$$\begin{aligned} \hat{H}_0|0\rangle &= E_0|0\rangle \\ \hat{H}_0|1\rangle &= E_1|1\rangle \end{aligned} \tag{1.2.1}$$

Turning on a perturbation $\hat{W} = \hbar\Omega(t)\cos(\omega t)\,\hat{\sigma}_x$ by an external driving field[1] where $\Omega(t)$ is a slowly changing envelope, ω is the field's frequency and $\hat{\sigma_i}$ are the pauli matrices, the Hamiltonian can be expressed by a 2×2 matrix of the form:

---

[1] This is not the most general kind of perturbation. Adding a $\hat{\sigma}_z$ term merely changes the eigenenergies and $\hat{\sigma}_y$ changes the phase of the field relative to the system.

$$\hat{\mathcal{H}} = -\frac{\hbar\omega_0}{2}\hat{\sigma}_z + \hbar\Omega\left(t\right)\cos\left(\omega t\right)\hat{\sigma}_x \tag{1.2.2}$$

where $\omega_0 = \frac{E_1 - E_0}{\hbar}$. Since the term $\mathbf{\Omega}\left(t\right)\cos\left(\omega t\right)$ typically changes very rapidly in time, it is useful to transform the Hamiltonian to a rotating frame of frequency ω. In this frame $\hat{\tilde{\mathcal{H}}} = -\frac{\hbar\Delta}{2}\hat{\sigma}_z + \frac{\hbar\Omega(t)}{2}\left(1 + e^{i2\omega t}\right)\hat{\sigma}_x$ where $\Delta = \omega_0 - \omega$ is the detuning. Since the last term of the perturbation reverses itself very rapidly while the other slowly accumulates over time, the fast part can be ignored. This approximation is referred to as the rotating wave approximation (RWA). The time dependence of these operators is determined by the Heisenberg equation: $i\hbar\dot{\hat{\boldsymbol{\sigma}}} = \left[\hat{\boldsymbol{\sigma}}, \hat{\tilde{\mathcal{H}}}\right]$. The equations for the dynamics of the pauli operators can be transformed to semi-classical equations describing the precession of a solid body acted on by a known torque [13]:

$$\frac{d}{dt}\boldsymbol{r} = \mathbf{\Omega} \times \boldsymbol{r} \tag{1.2.3}$$

where $\mathbf{\Omega} \equiv \left(\Omega\left(t\right), 0, \Delta\right)$[2] and $\boldsymbol{r} = \left(u, v, w\right)$ is the pseudospin vector in the transformed coordinate frame. w is the level population difference: $w = -1$ corresponds to the system being in the ground state and $w = 1$ the opposite. The "pseudospin" vector $\boldsymbol{r}\left(t\right)$ precesses about the torque vector $\mathbf{\Omega}\left(t\right)$ thereby tracing out an orbit on a unit sphere named the *Bloch* sphere (see Fig. 1.1).

1.2.1 Rabi Oscillations

The simplest solution to equations 1.2.3 is when $\Delta = 0$ and the system is exactly at resonance with the external field. Defining $\theta\left(t\right) = \int_{-\infty}^{t}\Omega\left(t'\right)dt'$ the

---

[2] In the most general case, the drive can take an arbitrary phase ϕ_d and $\mathbf{\Omega} = \left(\Omega\cos\phi_d, \Omega\sin\phi_d, \Delta\right)$.

solution is[13]:

$$\boldsymbol{r} = \left(u_0, w_0 \sin\theta\left(t\right) + v_0 \cos\theta\left(t\right), -v_0 \sin\theta\left(t\right) + w_0 \cos\theta\left(t\right)\right) \tag{1.2.4}$$

In the case of a constant field envelope with a steady value Ω between t_1 and t_2, $\theta = \Omega\left(t_2 - t_1\right)$. $\Omega/2\pi$ is called the Rabi frequency which is the rate of coherent oscillations between the two levels. If the system is in its ground state and a square pulse of duration Δt is applied such that $\Omega\Delta t = \pi$, the system finishes in its upper state. This is called a $\pi - pulse$ since it refers to a rotation on the Bloch sphere of $\theta = \pi$ (Fig. 1.2.3).

Detuning. If $\Delta \neq 0$, $\boldsymbol{\Omega}$ is on the **x-z** plane and the precession is more complex. When dealing with a square pulse of amplitude Ω and the system is initially in its ground state, the solution for w is:

$$w\left(t;\Delta\right) = -1 + \frac{2\Omega^2}{\Omega^2 + \Delta^2}\sin^2\left(\sqrt{\Omega^2 + \Delta^2}\frac{t}{2}\right) \tag{1.2.5}$$

The oscillation frequency increases but the excited population decreases with Δ. The eigenenergies are given by $E_\pm = \pm\frac{1}{2}\sqrt{\Omega^2 + \Delta^2}$.

Decoherence. Decoherence is incorporated into the theory by adding the following term to Eq. 1.2.3:

$$\boldsymbol{\Gamma} = \left(-u/T_2, -v/T_2, -\left(w - w_{eq}\right)/T_1\right) \tag{1.2.6}$$

T_1 is a phenomenological constant that accounts for the energy damping in the absence of a driving field and T_2 represents interactions, such as collisions in a gas which can distrub the resonant oscillations without disturbing the system's energy. w_{eq} represents the excited population in equilibrium due to a thermal reservoir or other sources that input energy to the system in an incoherent manner. In general, $T_2 \leq 2T_1$ in order to keep the norm of the bloch vector maximally bounded by unity. When dealing with decoherence the state is no longer represented by state vector but rather by a density matrix which in the formulation given here is expressed by: $\hat{\rho} = \frac{1}{2}\left(\hat{I} + \boldsymbol{r} \cdot \hat{\boldsymbol{\sigma}}\right)$ where $\hat{I}$ is the identity matrix. Decoherence causes the Bloch vector to point inside the Bloch sphere[1]. The equation can be solved analytically in the case of a steady field Ω and is naturally more complex. In the long-time steady-state case ($\dot{\boldsymbol{r}} = \boldsymbol{0}$) the solution is:

$$\begin{pmatrix} u \\ v \\ w \end{pmatrix} = \frac{w_{eq}}{1 + \left(\Delta T_2\right)^2 + T_1 T_2 \Omega^2} \begin{pmatrix} -\Delta\Omega T_2 \\ \Omega T_2 \\ 1 + \left(\Delta T_2\right)^2 \end{pmatrix}. \tag{1.2.7}$$

As stated in the equation, the population difference w is a lorentzian as a function of detuning with a width of: $\Delta_{FWHM} = 2\sqrt{\frac{1+T_1T_2\Omega^2}{T_2^2}}$. In the weak field case, $\Omega \ll \frac{1}{\sqrt{T_1T_2}}$, the width becomes $\Delta_{FWHM} = \frac{2}{T_2}$ and its measurement can be a convenient way to determine the coherence time T_2. In the strong field case, the resonance peak is broadened: $\Delta_{FWHM} = 2\Omega\sqrt{T_1/T_2}$.

1.2.2 Avoided Level Crossing

A plot of the eigenenergies in the presence of a driving field as a function of the detuning is shown in Fig. 1.2. Without the presence of the drive one can observe the degeneracy of the two levels at resonance . This degenerecy is lifted when the drive is turned on and the difference in energy between the two levels at resonance is given by $\hbar\Omega$. this effect is seen with spectroscopic measurement on the Josephson phase qubit when it couples to two level systems and will be discussed in Sec. 2.3.3.

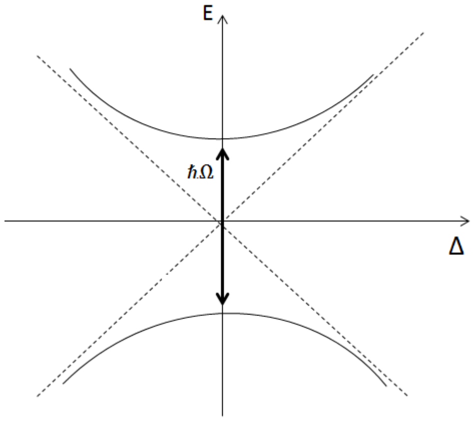

Fig. 1.2: Avoided level crossing. Solid line: in presence of drive field. Dashed line: without drive.

1.3 Superconducting Qubits

1.3.1 Superconductivity and the Josephson effect.

The effect of a dissipation-free electrical current was discovered by Onnes in 1911 at Leiden when he noticed that the electrical resistance of mercury dropped to zero for temperatures below a critical point of 4 K. This peculiar phenomena was later discovered in other metals al low temperatures. In the year 1933, Meissner and Ochsenfeld discovered that magnetic fields are expelled from superconductors when cooled below their critical temperatures[14]. These discoveries have driven the curiosity of many physicists who tried to explain the mechanism for the effect. Various phenomenological models have been proposed during the 30′s and 40′s. One distinct model is that of F. and H. London who introduced the London equations[15]:

$$\overrightarrow{E} = \frac{\partial}{\partial t}\left(\Lambda \overrightarrow{J_s}\right) \tag{1.3.1}$$

$$\overrightarrow{h} = -c\overrightarrow{\nabla} \times \left(\Lambda \overrightarrow{J_s}\right) \tag{1.3.2}$$

where $\Lambda = \frac{4\pi\lambda^2}{c^2} = \frac{m_e}{n_s e^2}$, m_e is the superconducting electron mass, n_s is the number density of superconducting e^- and $\overrightarrow{J_s}$ is the superconducting current. The first equation is derived from the Drude model assuming an infinite mean free path. The second equation, together with maxwell's equation $\overrightarrow{\nabla} \times \overrightarrow{h} = \frac{4\pi\overrightarrow{J}}{c}$ derives the screening of the magnetic field inside the superconductor with a typical London penetration depth λ in accordance with the Meissner effect.

It was only in 1957 that Bardeen, Cooper and Schreiffer (BCS) suggested a microscopic theory that accounts for all of the properties of superconductivity discovered during the years[16]. As stated in the theory, below a critical temperature (T_c), electrons pair into a so called *Cooper pair* under the influence of phonon-induced coupling. The Cooper pairs form a coherent condensate that can be described by a complex wavefunction Ψ, the superconducting order parameter, introduced by Ginzburg and Landau in 1950 as part of their phenonomenological theory for superconductivity as a second-order phase transition[17].

In 1962, Josephson has predicted that when two superconductors are separated with a thin dielectric barrier named a *Josephson junction*, a macroscopic Cooper pair current will tunnel through the barrier due to the overlap of the superconducting wavefunctions[18]. The current depends on the phase difference of the order parameters between the two wavefunctions and is given by the first Josephson equation:

$$I = I_0 \sin\varphi \tag{1.3.3}$$

where $\varphi = \phi_1 - \phi_2$ is the phase difference and I_0 is the maximum current that can flow without dissipation and depends on the superconducting energy gap Δ and the normal, Ohmic resistance of the tunnel barrier. The second Josephson equation relates the time evolution of the phase difference φ to the voltage across the junction:

$$\frac{d\varphi}{dt} = \frac{2e}{\hbar}V = \frac{2\pi}{\Phi_0}V \tag{1.3.4}$$

where h is planck's constant and Φ_0 is the flux quantum. Using the standard definition of inductance, $L = V/\left(\frac{dI}{dt}\right)$, the inductance of the Josephson junction $L_J = \frac{\hbar}{2eI_0 \cos\varphi}$ is non-linear. The Josephson junction has a main role in the design of superconducting qubits due to the fact that it is a non-linear, non-dissipative element. The application of these two important properties will be described in the following sections.

1.3.2 Quantum Electrical Circuits

While macroscopic quantum phenomena such as superconductivity and superfluidity were understood in the framework of quantum mechanics, it was not clear whether macroscopic objects can behave quantum mechanically. In the 1980's, John Clarke and others have shown that a supercurrent can tunnel through a phase barrier, thus demonstrating the first purely quantum effect in an electrical circuit [19, 20]. Phase and charge were shown to be conjugate quantum variables experimentaly and theoretically using the method of second quantization[21].

Additional experiments have shown Rabi oscillations [22], Bell violations [23], entanglement [24, 25] in superconducting electrical ciruits, setting them as a favorite candidate for a qubit. In this thesis two kinds of qubits were used: the phase and transmon qubits. While sharing the same building blocks, each one has its own method of operation and measurement. The following sections review both qubits, their advantages and disadvantages.

1.3.3 Flux-Biased Josephson Phase Qubit

Josephson junctions under certain conditions can be modeled by the RSCJ model introduced by Stewart and McCumber [26, 27]. In order to account for the junction's effective shunt resistance and its capacitance, an equivalent circuit consisting of a resistor, capacitor and the junction in parallel is used. Using Kirchoff's law, the total current flowing through the system is given by the sum of currents from each path:

$$I = I_0 \sin\varphi + \frac{V}{R} + C\frac{dV}{dt} = I_0 \sin\varphi + \frac{1}{R}\frac{\Phi_0}{2\pi}\frac{d\varphi}{dt} + C\frac{\Phi_0}{2\pi}\frac{d^2\varphi}{dt^2} \tag{1.3.5}$$

Where $\Phi_0 = h/2e$ is the flux quantum, R is the resistance and C the capacitance. This equation resembles a particle moving in an effective potential $U(\varphi)$ with a friction force and can be written as:

$$m\frac{d^2\varphi}{dt^2} + \frac{m}{RC}\frac{d\varphi}{dt} + \frac{\partial U(\varphi)}{\partial\varphi} = 0 \tag{1.3.6}$$

where $m = C\left(\frac{\Phi_0}{2\pi}\right)^2$ is the particle effective mass and the effective potential is: $U(\varphi) = E_J\left(-\frac{I}{I_0}\varphi - \cos\varphi\right)$; $E_J = \frac{I_0\Phi_0}{2\pi}$ is the Josephson energy.

When there is no bias current through the junction $(I = 0)$, the equation is equivalent to that of a pendulum and for low amplitudes has an oscillation frequency of $\omega_0 = \sqrt{\left(\frac{d^2U}{d\delta^2}\right)_{\delta=\delta_0}/m} = \sqrt{\frac{I_0^2\cos\delta_0}{E_J C}} = \omega_p\sqrt{\cos\delta_0}$ and ω_p is typically designed to be in the GHz range. For $I < I_0$ the potential becomes asymmetric and is tilted by the linear phase term, with a tilt slope determined by I. The Hamiltonian can be solved in the case of a shallow well $(I \lesssim I_0)$ and the transition energies are obtained in the washboard potential well, the first transition

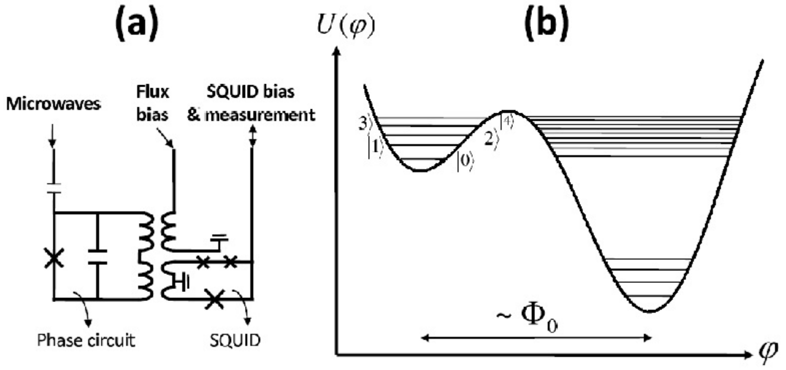

Fig. 1.3: The Josephson phase qubit. (a) Circuit diagram: the junction is inductively coupled to flux bias current and measured using a SQUID. Qubit is excited using microwave pulses. (b) Typical working potential: the left well is excited and manipulated and then measured via selective tunneling to the right well.

energy given by[28]:

$$\omega_{01} = \omega_p \left(1 - \frac{5}{36}\frac{\hbar\omega_p}{\Delta U}\right) \tag{1.3.7}$$

where $\Delta U = 2\sqrt{2}\frac{I_0\Phi_0}{3\pi}\left(1 - \frac{I}{I_0}\right)^{3/2}$ is the current dependant potential barrier (see Fig. 1.4a).

A direct current bias connected to the junction will make the circuit sensitive to bias current noise and increase its decay rate. To eliminate these effects, the circuit is biased using an inductively coupled line[29] (see Fig. 1.3a). The current I_q circulating through the qubit loop with inductance L contributes a magnetic energy term to the circuit Hamiltonian: $E_M = \frac{1}{2}LI_q^2$. The flux through the qubit is: $\Phi_q = \Phi_{ext} + LI_q$ where Φ_{ext} is the external flux from the flux bias line. Flux quantization constrains the phase difference to be $\varphi = 2\pi\Phi_q/\Phi_0$ and thus $I_q = \frac{\varphi\Phi_0}{2\pi} - \Phi_{ext}$. The magnetic energy term replaces the bias current term in the effective potential and this leads to the following Hamiltonian for the

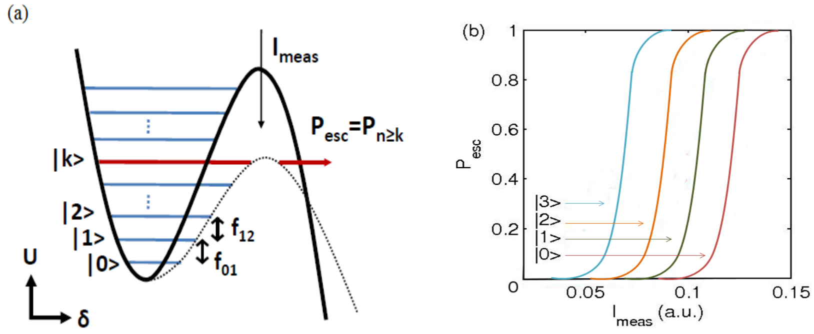

Fig. 1.4: Qubit measurement. (a) State population in the left well tunnels to the right well when the potential barrier lowers due to a measurement pulse. (b) Tunneling probability as a function of bias current. Higher levels require lower bias currents to tunnel outside the well.

flux-biased phase qubit:

$$\mathcal{H} = -\frac{2e^2}{C}\frac{d^2}{d\hat{\varphi}^2} - E_J \cos\hat{\varphi} + \frac{1}{2L}\left(\Phi_{ext} - \frac{\hat{\varphi}\Phi_0}{2\pi}\right)^2 \tag{1.3.8}$$

For $LI_0 > \Phi_0/2\pi$ the qubit potential has more than one minima. The number of minima increases with the value of LI_0 but typical circuit designs are fabricated to have two minimas at the most which is what is needed for the qubit manipulation and measurement. For certain flux values, one can obtain the potential diagram in Fig. 1.3b. After reset, the qubit is in the ground state of the shallow well.

The amount of energy levels in the well is determined by the flux bias and can be in the range of 1 to ~ 50. In the shallow well, the qubit can be excited by resonant microwave pulses. While typically only the bottom two levels are used as the qubit, the experiments presented in this work make use of higher levels in the well. The qubit is then measured by tilting the potential well using a short but still adiabatic dc-flux pulse in order to force the population above a certain level to tunnel to the right well (Fig. 1.4). Since tunneling is exponentially sensitive to the barrier height, each level can be measured separately via selective tunneling [22]. After a tunneling event occured which causes the qubit flux Φ_q to change by $\sim \Phi_0$, the change in flux is measured by the change of critical current of a superconducting quantum interference device (SQUID)[30, 31] which is inductively coupled to the qubit circuit as well (Fig. 1.3a).

1.3.4 Transmon Qubit

The transmon qubit consists of a superconducting wire which is coupled to the external circuitry by two Josephson junctions, namely a split Cooper-pair box. The two junctions close a loop, allowing for the tuning of the Josephson energy by an external magnetic flux in a way analogous to a SQUID (see Fig. 1.5a). This design is closely related to the Cooper pair box [32] except the additional large shunting capacitance of the two Josephson junctions accompanied by a similar increase in gate capacitance to the transmission line. The qubit Hamiltonian is[33]:

$$\hat{\mathcal{H}} = 4E_C(\hat{n} - n_g)^2 - E_J\left(\Phi\right)\cos\hat{\varphi} \tag{1.3.9}$$

where E_C is the charging energy, n_g the offset charge, Φ the external flux and $\hat{n}$ and $\hat{\varphi}$ denote the number of Cooper pairs transferred between the islands and the gauge-invariant phase difference between the superconductors, respectively. The wavefunctions and eigenenergies can be solved exactly in the phase basis in terms of Mathieu functions. Fig. 1.5(b-c) show the lowest three energy levels as a function of the effective offset charge n_g for different E_J/E_C ratios. As can be seen, the anharmonicity decreases and the energy variation in respect to charge, namely charge dispersion, rapidly decreases with the increase

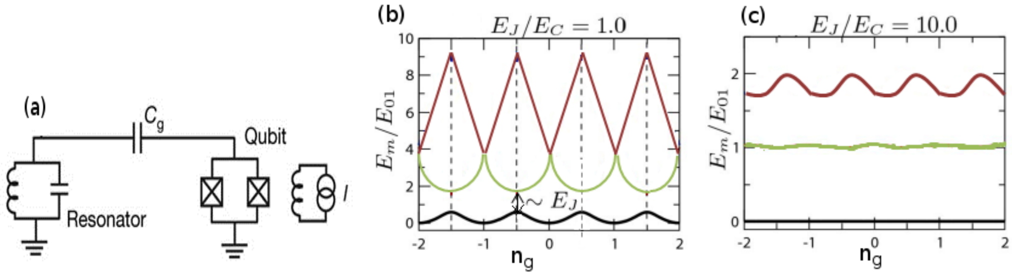

Fig. 1.5: (a) The transmon qubit. A split Cooper pair box tunable by a bias current I is capacitively coupled to a resonator. (b-c) Eigenenergies E_m as a function of offset charge n_g for the first three levels with different E_J/E_C ratios.

of E_J/E_C. The susceptability of the qubit to noise increases with charge dispersion while lower anharmonicity can be a problem when controlling the qubit by the excitations of unwanted levels. While the anharmonicity decreases by a weak power law, the charge dispersion decreases exponentially as function of E_J/E_C[33]. Consequently, The transmon is operated at this regime, in contrast with the Cooper pair box.

The transmon shares similar properties with the phase qubit such as the large E_J/E_C ratio (transmon $\sim 10^2$, phase $\sim 10^4$) and the insensitivity to charge noise. The crucial difference between the two is the DC connection between the two sides of the junction in the phase qubit that makes the states of φ and $\varphi + 2\pi$ physically distinct as opposed to the transmon qubit in which the phase is compact.

The transmon eigenstates are not pure charge states. The eigenstates spread over an increasing number of charge states with increasing E_J/E_C, hence a measurement cannot be done in that basis, unlike the charge qubit[32]. It was found that embedding the transmon in a 1-D transmission line cavity provides the ability of measurement in the qubit. In addition, it protects the qubit from radiative decay by filtering out unwanted electromagentic modes that can cause spontaneous decay. The qubit-cavity Hamiltonian including the

RWA which eliminates terms that do not preserve the number of excitations in the system is described by the Jaynes-Cummings model[34, 35]:

$$\hat{\mathcal{H}}_{JC} = \hbar\omega_r \left(\hat{a}^\dagger\hat{a} + 1/2\right) + \frac{\hbar}{2}\omega_q\hat{\sigma}_z + \hbar g\left(\hat{a} + \hat{a}^\dagger\right)\hat{\sigma}_x \tag{1.3.10}$$

where ω_r and ω_q are the cavity and qubit frequencies, respectively and g is the coupling strength. When $\omega_q = \omega_r$, the resonant regime, the eigenstates are equal superpositions of qubit and cavity states. When the qubit and cavity are far detuned ($g/\Delta \ll 1$ where $\Delta = \omega_q - \omega_r$) they can no longer exchange energy. Alternatively, they interact via a *dispersive* interaction that slightly changes the energy levels. Eq. 1.3.10 can be expanded in powers of (g/Δ) yielding the dispersive Hamiltonian[34]:

$$\hat{\mathcal{H}}'_{JC} \approx \hbar\left(\omega_r + \chi\hat{\sigma}_z\right)\hat{a}^\dagger\hat{a} + \frac{\hbar}{2}(\omega_q + \chi)\hat{\sigma}_z \tag{1.3.11}$$

where $\chi = g^2/\Delta$. The cavity frequency is therefore qubit state dependant and vice versa.

The qubit is measured in the dispersive regime by transmitting a coherent drive through the cavity in order to determine the cavity frequency. The phase or amplitude of the transmitted signal is dependant on the cavity frequency which in turn depends on the qubit state.

1.3.5 Decay and Decoherence in Superconducting Circuits

Experimental quantum systems are never isolated completely from the environment. The quantum nature of the qubit state is disturbed by the interactions with the surrounding environment. Decoherence in superconducting qubits is associated with dielectric loss, noise and dissipation in the control wiring of the qubit, $1/f$ flux noise, two-level defects in the junction oxides and quasiparticle excitations. Some of these mechanisms can cause energy relaxation in the qubit state which is related to the decay of the diagonal elements in the density matrix and others cause the loss of coherence of superposition states. The initial pure state thus evolves to a mixed state and loses its quantum properties. These mechanisms are reviewed in this section for both transmon and phase qubit samples.

1.3.5.1 Energy relaxation mechanisms

Dielectric Loss. This was found to be the dominant source for energy decay in superconducting qubits and is attributed to energy relaxation of electric dipoles in the dielectric materials used in qubit samples for capacitors and Josephson junctions[36]. Due to its large capacitance, the phase qubit suffers mostly from this loss mechanism. The device electrical wiring is typically made of aluminum since its oxide is used as the junction tunnel barrier and has relatively low loss. However, the amorphous oxide can still limit the the decay time. Using its crystaline form, sapphire, which has a lower loss as the tunnel barrier has been the subject of recent research [37, 38]. Alternatively, the use of microbridges which does not involve dielectrics can be used instead tunnel barriers [39]. Recent work has been done to fabricate a transmon qubit with microstrip lines instead of the commonly used coplanar transmission lines, resulting in improved relaxation times [40].

Quasi-particles. In a superconductor well below the critical temperature, quasiparticles are exponentially supressed due to the superconducting gap Δ. However, an experiment on a Cooper pair box measured a relatively large quasiparticle density of $\sim 10\ \mu m^{-3}$[41]. Possible sources for the measured quasiparticles are themal radiation from higher stages in the fridge and local heating from SQUID switching. The measured density was used to calculate a decay time of $T_1 = 2\ \mu s$ for typical phase qubits[42].

Control and measurement circuitry. A superconducting qubit is generally coupled to control circuitry via a dissipationless element, typically a capacitor or a mutual inductance. An admittance $Y_1(\omega)$ is associated with the external circuitry and transformed to an admittance $Y_2(\omega)$ seen from the qubit. Dissipation is calculated by the real part of the admittance of the external circuit by a simple current transformation and the fluctuation-dissipation theorem [43]: $Re\left[Y_2(\omega)\right] = \left(dI_2/dI_1\right)^2 Re\left[Y_2(\omega)\right]$ where $I_2(I_1)$ is the current transfer function between the qubit and the external circuit. This means that when fluctuations in I_1 produce no currents I_2 in the qubit, there is no dissipation to the environment.

The purcell effect. The transmon qubit is placed inside a resonator that changes its spontaneous emission rate which is known as the Purcell effect [44]. In the absence of photons in the cavity the excited transmon decays at a rate of $\gamma_\kappa = \kappa\frac{g^2}{\Delta^2}$ through the cavity [33]. Near the cavity resonance, the purcell effect enhances qubit relaxation but in the dispersive regime, the cavity protects the qubit from decay and the relaxation time is considerably longer than expected for relaxation into the continuum [45]. The transmon is operated at negative detunings from the cavity to prevent spontaneous emission modes due to higher modes in the cavity [45].

1.3.5.2 Decohrence mechanisms

Flux Noise. Since bias currents control the qubit, bias noise fluctuates the qubit state and causes decoherence I[46]. Noise at low frequency in the macroscopic parameters I_0 and Φ_{ext} randomly rotates the Bloch vector around the $\hat{z}$ axis due to $\hat{\sigma_z}$ operations. These rotations randomly change the phase $\phi = \int \omega_{01}(t)dt$ of the qubit state. Since every measurement is averaged several hundred times to determine occupation probabilities and the qubit phase slightly changes between measurements, the state becomes indistinguishable from a statistical mixture. It was found experimentally that noise in Φ_{ext} is dominant in the phase qubit system by comparing the noise at positive and negative bias in the phase qubit[47]. The noise was found to have a $1/f$ power spectrum and an extrapolated amplitude of $S_\Phi(1Hz) = 4\mu\Phi_0/\sqrt{(Hz}$ which is comparable with a previous measurement of $1/f$ noise on SQUIDs[48]. The scaling and amplitude of the noise are found to be weakly dependant on the geometry or material of the sample and its origin is thought to be due to magnetic spin defects on the surface of the superconducting electrodes[49, 50]. Spin echo techniques can effectively decrease this low frequency noise[46]. In the transmon qubit, operating at the flux "sweet spot" can improve coherence times [33].

Two Level Defects. The qubit can coherently couple to two level states (TLS's)[51] which are defect states in the oxide layer or dielectrics and these can in turn couple to degrees of freedom in the dielectric and cause energy decay and loss of coherence in the qubit. They can be reduced by using smaller junctions and fabricating epitaxially grown junctions [37, 38]. They can be avoided by biasing the qubit far from their transition energy.

CHAPTER 2

Measurement Apparatus and Methods

2.1 Cryogenics and Filtering

To observe the quantum properties of superconducting qubits, the thermal energy has to be much lower than the energy separation between the qubit levels $\hbar\omega_{01}$. The qubit is therefore cooled to a temperature of ~ 10 mK. The cooling method and noise filtering is described in this chapter.

2.1.1 The Dilution Fridge

In order to cool the electrical samples, an Oxford VeriCold Dr-200 dilution fridge is used. An extensive explanation of the operation of dilution refrigerators is given in [52, 53, 54]. The dilution process utilizes the phase separation that occurs in a mixture of $^3He -^4 He$ at temperatures below 0.87 K where two layers of liquid form: a ^3He rich one floating on top of the ^4He rich phase. The ^4He is in its superfluid phase while ^3He is a normal fluid. The ^3He is pumped from the ^4He rich phase which drives the system out of equilibrium and is then evaporated in a heated distillery to separate it from ^4He. In order to return to equilibrium, ^3He from the top part of the mixing chamber (MC) has to cross the phase boundary. Since the enthalpy of ^3He in the ^4He rich phase is higher, the ^3He on top absorbs heat from the environment and crosses the boundary. The process thus cools the walls of the mixing chamber that are in thermal contact with the refrigerator plate. The dilution process stops at 3 mK[1] since ^3He atoms pair-up to form a superfluid.

The precool stage is done by a Cryomech pulse tube system with a rotary valve[55, 56] which cools all stages of the fridge to ~ 4 K. The mixture is then compressed into a $\sim 1mm$ tube where it is condensed through the Joule-Thomson process. The process continues to ~ 800 mK when the dilution cycle begins. The fridge plates: 70 K, 4 K and still plate are thermally isolated from one another. In order to prevent radiation heating the different plates, three metal cans are used to screen radiation between each stage. The fridge is covered in a vacuum chamber which can hold pressures as low as $\sim 10^{-6}$ torr to reduce thermal conductivity to the sorroundings. Three outer cans made from an iron-nickel-copper alloy with a high magnetic permeability (few 10^4) cover the fridge to supress external magnetic fields which can affect the flux in the circuit and cause dephasing. The mixing chamber plate temperature is monitored with a ruthenium-oxide resistor, calibrated down to a few mK with ^{60}Co nuclear thermometry. All temperatures in the fridge are measured using a 4-wire Lakeshore resistance bridge.

2.1.2 Electrical Wiring

Semi-rigid coaxial SMA cables are used to transfer electrical signals from room temperature electronics to the fridge. These cables can transfer signals up to ~ 20 GHz. The cables from room temperature to the 4 K plate are made from stainless-steel which has low thermal conductivity. The cables from the 4 K plate to the still and mixing chamber plate are made out of Neobium which is

---

[1] Our fridge reaches 20 mK.

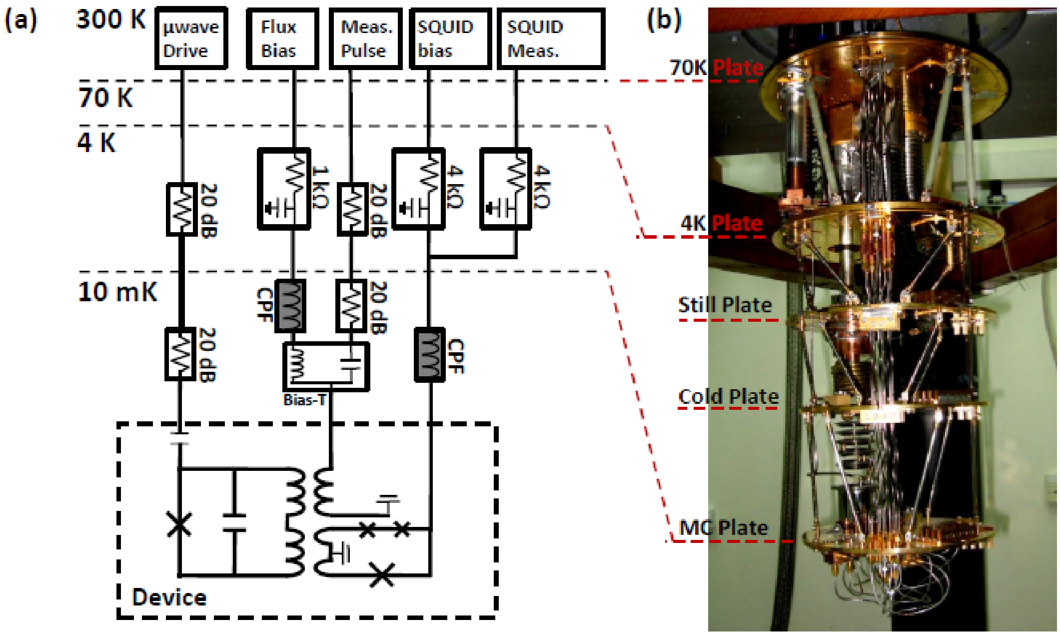

Fig. 2.1: Experimental set up for phase qubit measurement - (a) Coaxial cables and filtering in each fridge plate. (b) Photo of the fridge.

superconducting under 9.3 K and has an exponentially vanishing thermal conductivity. Coaxial cables are thermally anchored to the 4 K stage via filters and attenuators[2] and additional attenuation is used in the MC plate. Thermalizing the coaxial cables reduces heat load on the cold plates and prevents Johnson noise from reaching the sample, thus decreasing decoherence mechanisms. Attenuators have $\sim$ 100 Ω resistance from centerpin to ground which provides sufficient thermal conductivity. In addition, attenuators are used to increase SNR since thermal (Johnson) noise is decreased while the thermal noise added due to the finite temperature of the attenuators at the cold stages is low. Low-pass filters include a split series resistance (4 $k\Omega$ for the SQUID lines and 1 $k\Omega$ for the flux bias line) and 300 pF split capacitance to ground which attenuates noise above 1 MHz. Filters are filled with thermal grease from centerpin

---

[2] Center-pin of coaxial cables is insulated from the ground by teflon.

to ground to increase thermal conductivity. They are used for the flux and SQUID bias and SQUID measurement in order to transfer the voltage created by the fast-bias card and the GHz DAC into bias currents and screen high frequency noise that can cause decoherence. Since these filters stop attenuating above 200 MHz, special filters made of a coil immersed in an non-conductive epoxy copper- powder mix are used. RF radiation (above & 100 MHz) is absorbed in these filters by plasmons on the surface of the fine copper grains (10 mm), and provide high attenuation (60 dB) up to 15 GHz ([57], Sec. 3.3.1). The flux bias line needs to accomodate both low and high frequency signals corresponding to qubit bias and measurement pulse. These signals are combined in a bias-tee, which has two inputs: a high-frequency port with a capacitor in series to prevent leakage of low frequency signals and a low-frequency port with an inductor to prevent leakage of high frequency signals. The bias tee used in the experiment has no capacitor because the device itself has a capacitance to ground. The inductor used is a Mini-Circuits ADCH-80 RF-choke with 7 mH inductance which provides $\sim$ 7 GHz bandwidth for the measurement pulse channel. Experimental set-up for the phase qubit is shown in Fig. 2.1.

2.2 Pulse Synthesis

In order to coherently control and manipulate the qubit, it is necessary to create electrical pulses in the GHz range with nano-second resolution and a high on-off ratio. In addition, synchronised bias voltage for both qubit and SQUID and means to measure the SQUID's critical current are needed for qubit operation and measurement. In order to achieve that we use FPGA-based customized electronics which was designed by the Martinis group in UCSB [58]. In the following section the electronic setup will be reviewed briefly, detailed infor-

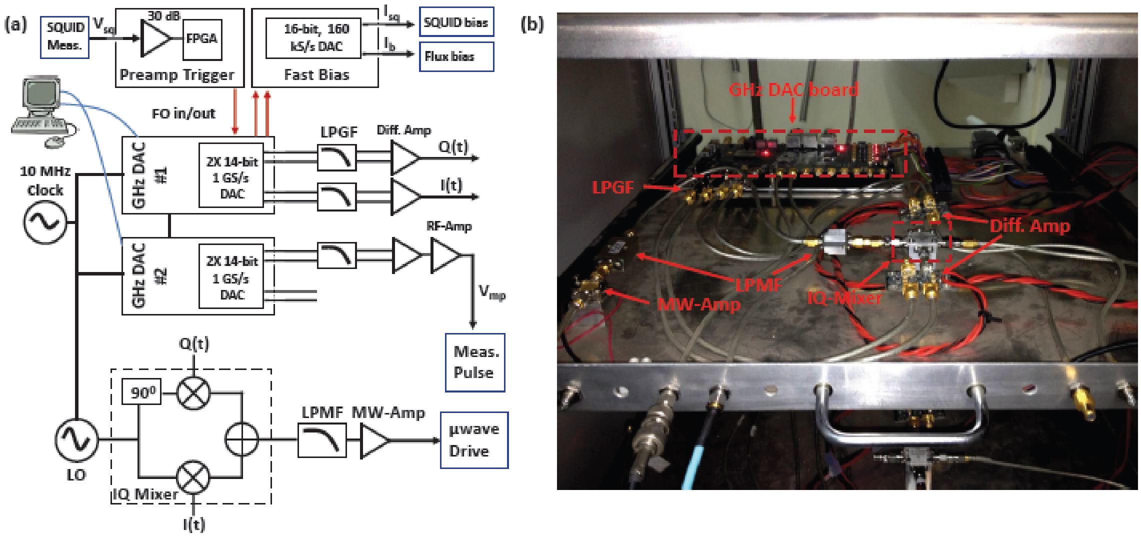

Fig. 2.2: (a) Schematics of the electronic set-up. Top: Low-frequency DAC used for biasing and preamp card for SQUID measurement. Bottom: GHz DAC chain used for coherent control and measurement of the qubit. (b) Photo of the GHz DAC chain.

mation can be found in ([59], Sec. 2.2.4).

Electronic pulses are produced by the GHz DAC chain which consists of a GHz digital to analog converter board, Anritsu MG3692B local oscillator (10MHz - 20 GHz), differential amplifiers, IQ mixer and filters. Schematics of the electronics set-up is shown in Fig. 2.2. The GHz DAC board has two 14-bit digital to analog converters which are used to generate output waveforms at a sampling rate of 1 GHz with a programmable sequence of length 8192 (8.192 μs). Each converter produces a 0 V - 0.5 V signal at 50 Ω in two channels $V^+$and V^- related by $V^- = 0.5V - V^+$. The two channels are connected to a differential amplifier which outputs two identical signals in the range $-0.25V - 0.25V$. 10 MHz clock input allows an arbitrary number of cards to be synchronized together. The bandwidth of the DAC is 500 MHz, limited by the Nyquist frequency and is further reduced by dissipative gaussian filters[3] to eliminate clock feedthrough and aliasing problems. Consequently, the output impulse response is a 1.6 ns FWHM gaussian pulse. The DAC boards are connected via ethernet to a computer to receive pulse sequences and biasing commands and to send information about switching events of the SQUID.

Microwave pulses are generated by modulating the local oscillator using a Marki IQ mixer[4] with the two DAC channels serving as the $I(t)$ and $Q(t)$ channels. The mixer splits the local oscillator signal, one is multiplied with a signal $I(t)$ and the other is phase shifted by $90°$ and multiplied with a signal $Q(t)$. The two signals are combined and the output is: $\sqrt{I(t)^2 + Q(t)^2} cos \left(2\pi f_{LO} t + \phi(t)\right)$ where $\phi = \arctan\left(Q(t)/I(t)\right)$. This allows a control of both phase and amplitude in nanosecond resolution with the bandwidth limit of the DAC. A common use of this set-up is to modulate the frequency of the pulse $f_{LO} + f_{IF}$ to eliminate leakage of the oscillator in the measurements due to mixer imperfections and to perform chirp excitations as will be described in Sec. 3.2.4. There are four problems in a real IQ mixer that must be addressed in order to perform the experiment reliably: 1) the generation of LO harmonics; 2) local oscillator leakage at $I, Q = 0$; 3) cross-talk between the I and Q channels; 4) Ringing at the end of output pulses due to reflections from impedance mismatch.

LO harmonics are not modulated in the mixer and leak out to the output channel of the chain. This leakage may result in unwanted excitations in the system at sufficently large amplitudes and anharmonicity. They are corrected by a microwave low-pass filter with ~ -50 dB attenuation at the given frequency. LO frequency leakage is due to the mixer nonideality and is frequency dependant but can be corrected by searching for I, Q offsets that minimize the leakage for constant frequency intervals. This is done by an optimization algorithm using the large dynamic range of an N9020A Agilent spectrum analyzer.

---

[3] Custom built with a 3 dB point of 275 MHz

[4] Marki IQ0307LXP (3-7 GHz) and IQ0714LXP (7-14 GHz) are used.

The algorithm decreases the leakage power down to ~ -95 dBm which is 80 dB lower than the signal power. The ringing and cross talk are corrected using a custom two-channel numerical deconvolution technique that we developed[5].

Flux bias and squid bias voltages are produced by a fast-bias board. It has 4 low-noise channels with 16-bit resolution that can produce voltages in the range -2.5V - 2.5V with 25 $nV/\sqrt{Hz}$ noise. The board has an FPGA chip which is used to receive incoming commands from the GHz DAC by optical fibers and perform additional tasks. Once the SQUID is switched due to the applied bias current, a voltage develops on the junction (100 μV) which is amplified by $\sim 10^3$ using low noise amplifiers that are located on the Preamp-Trigger board. The board has 4 input channels, one for each qubit, with programmable low and high pass filters to remove noise from measurement[6]. The board also has an FPGA chip in order to send a trigger to the GHz DAC cards once the amplified voltage crosses a predefined threshold using a fiber optic cable. Both preamp and fast bias boards are powered using a couple of $+6$ V and -6 V batteries to eliminate noise from direct electrical connection to the ground.

2.3 Phase Qubit Measurement

2.3.1 Mapping of Phase Circuit Potential

The first step in measuring a phase qubit device is to map its potential. This enables the user to reset the qubit in a specific potential well where it decays into the ground state. The mapping is done by measuring the phase distribution as a function of Φ_{ext} after the qubit relaxes in the well. The time sequence is shown in Fig. 2.3a. At the beginning, Φ_{ext} is set to its maximal\minimal

---

[5] The method is described in appendix A.

[6] This noise is caused mostly by ground loops and coupled acoustic noise from the fridge

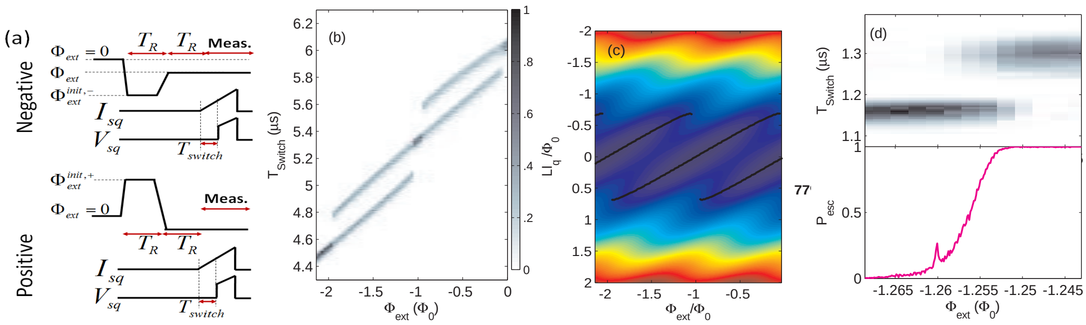

Fig. 2.3: Phase qubit potential mapping. (a) Experiment time sequence. (b) Phase distribution as a function of Φ_{ext}. (c) Calculated potential map as a function of Φ_{ext}, black lines represent potential minima. (d) Coexistence of two potential wells. Top: Overlap of switching time histograms, corresponding to two stable potential wells. Bottom: Tunneling probability as a function of Φ_{ext}.

value for a time T_R to ensure relaxation and is then adiabatically changed to the final value. This is done to ensure that occupation probability is distributed homogenously in all metastable wells. An increasing bias current is then applied to the SQUID to determine the switching time which is directly related to the SQUID critical current. The latter depends on the phase of the qubit that depends on the potential well in which the qubit is settled. The distribution of switching time is measured as a function of Φ_{ext} (Fig. 2.3b). The measurement was repeated for 300 times for each value of Φ_{ext}.The amount of metastable wells are dependant on the qubit inductance L, critical current I_0 and qubit capacitance C. In the qubit measured in this work, experimental parameters are: $L \approx 940\ pH$, $I_0 \approx 1.5\ \mu A$ and $C \approx 1.3\ pF$. The potential map is calculated for these parameters and shown in Fig. 2.3c. As can be seen, for each value of Φ_{ext} only two stable wells are present in agreement with experiment. The increase in switching time with branch number is attributed to the coupling between the qubit current bias and the SQUID, effectively adding to the measured flux.

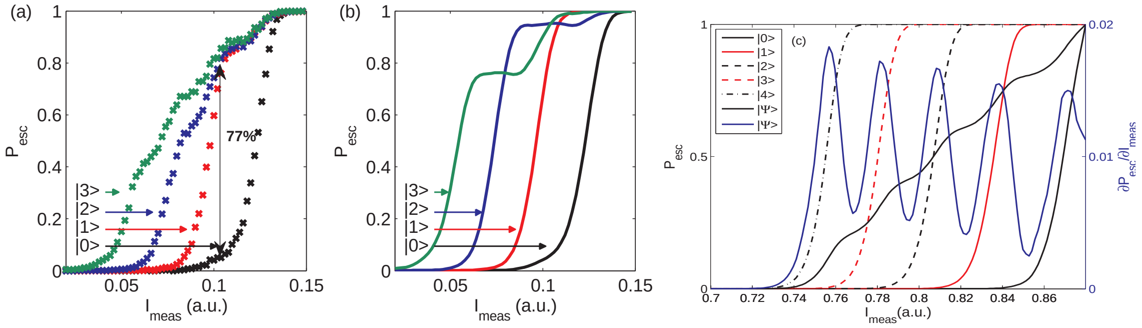

Fig. 2.4: Measured escape curves. (a) Measured escape probabilities as function of measurement pulse amplitude. The arrow represents the point of maximal visibility of 77% between ground and excited state (b) Normalized escape curves. (c) Left axis: escape curve of state $|\Psi\rangle = 1/\sqrt{5}\,(|0\rangle + |1\rangle + |2\rangle + |3\rangle + |4\rangle)$ (solid black). Right axis: escape curve derivative, the peaks correspond to positions of the 50% probability of the escape curve of each state.

2.3.2 Macroscopic Phase Tunneling Measurements

Qubit reset is done by applying a flux bias to a value where only one stable well is present corresponding to one branch where it left to decay to the ground state for a duration of $\sim 20\ \mu s$. As can be seen in Fig. 2.3b, two branches periodically overlap at a certain region. In this region macroscopic phase tunneling[20] from the shallow well to the deep well occurs due to the low barrier between the wells as depicted in Fig. 1.4. Fig. 2.3d shows the overlapping part of the branches, the transition from the shallow well on the left to the deeper well on the right increases due to the lowering of the barrier as a function of flux. One can set a switching time cutoff to calculate the probability of tunneling to the deeper well. At the bottom the tunneling probability is shown for the same measurement. The peak is associated to the effect of resonant tunneling[60].

As mentioned in Sec. 1.3.3, measurement is done by applying a pulse in the flux channel which adiabatically lowers the potential barrier. Fig. 2.4a shows the measured tunneling probabilities for different excited states as a function of measurement pulse amplitude. As expected, the tunneling probabilities for a higher excited state requires a lower measurement pulse due to the lower barrier. By applying a measurement pulse, one measures the cumulative tunneling probabilities of all levels that are higher than the lowered potential barrier. Using the escape probabilities of different pulses, information on the population in each level is gained. It is useful to set the measurement pulse amplitude at the value which gives the maximal measurement visibility as indicated by the arrow in Fig. 2.4a. The visibility decreases for higher excited states since the state preparation fidelity is lower. This is due to the shorter decay and decoherence times, excitations of unwanted levels as a result of the small anharmonicity (as seen from the steps in the escape curves) and possibly as a result of two-level defects[61].

To eliminate the contribution of the unwanted levels (see level $|3\rangle$ escape curve for example), escape curves can be normalized as shown in Fig. 2.4b. This is done by decomposing the measured escape curve into its single level building blocks. Defining $P_{esc}^{n}\left(I_{meas}\right)$ as the measured escape curve of level $|n\rangle$, normalization is calculated by finding the optimized solution P_n iteratively to the sets of equations $P_{esc}\left(I_{meas}^{j}\right) = \sum\limits_{n} P_n P_{esc}^{n}\left(I_{meas}^{j}\right)$ where I_{meas}^{j} is the j-th value of measurement pulse vector (x-axis in Fig. 2.4) of length J. In this work levels as high as 16 were measured in a low anharmonicity regime ($\beta = 22\text{MHz}$). Combining the short decoherence times of high excited states and the low anharmonicity, it is virtually impossible to prepare these states and measure their escape curves. In order to overcome this a chirp pulse (see Sec. 3.2.4) is applied which simultaneously excites many levels. The escape curve of the generated state is then measured. The escape curve's derivative with respect to I_{meas} is largest for a 50% tunneling probability. We utilize this property by calculating the derivative of the chirped escape curve, the peaks indicating the positions

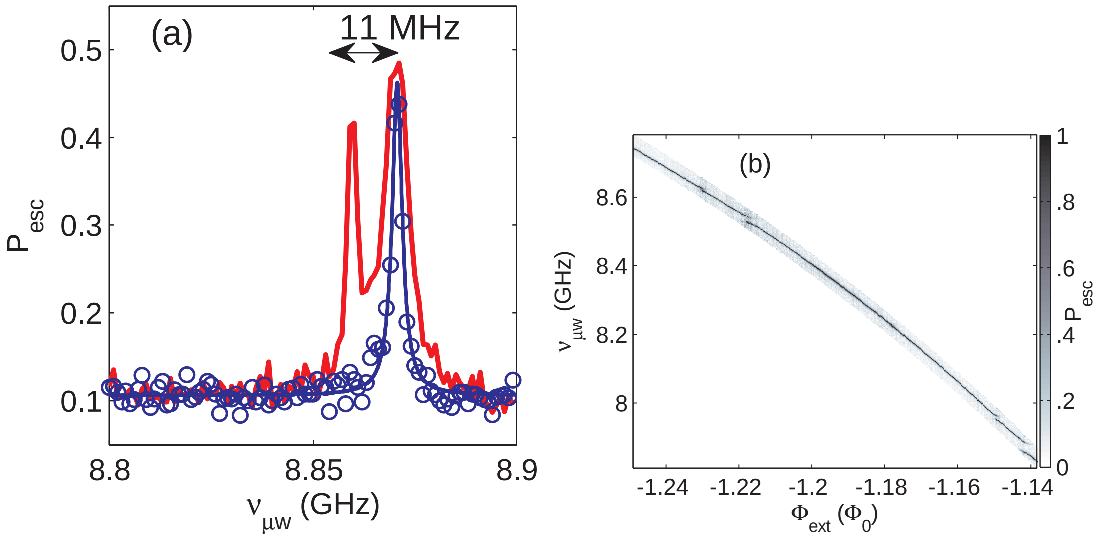

Fig. 2.5: Qubit spectroscopy. (a) Drive amplitude $\kappa\mathcal{E}_0/2\pi$=1.75 MHz (blue line) and $\kappa\mathcal{E}_0/2\pi$ = 4.375 MHz (red line). (b) Excited level probability as a function of frequency and Φ_{ext} showing avoided level crossing due to TLS.

of the higher levels escape curves as shown in Fig. 2.4c. The shape of the escape curve of higher levels are assumed to be identical to the first excited state curve, in agreement with WKB calculations of the tunneling rates.

2.3.3 Qubit Spectroscopy

Spectroscopic measurements are done using incoherent pulses of length τ ($\tau \gg T_2$) followed by a measurement pulse to determine excited state occupation probability . Fig. 2.5a shows an example of such a measurement. The blue line shows spectroscopy at a drive amplitude of $\Omega/2\pi = 1.75$ MHz where a single peak corresponding to the qubit resonance frequency is seen on $\nu_{01} = 8871$ MHz. The shape of the resonance is a Lorentzian with $\Delta\nu_{FWHM}$ =3 MHz corresponding to an inhomogenous coherence time of $T_2 = 1/\pi\Delta\nu_{FWHM} = 106$ ns (see Sec. 1.2) . The red line represents a measurement done with an amplitude higher by a factor of 2.5 and the broadening of the resonance peak is observed. Another peak is shown, 11 MHz apart which is attributed to a two-photon transition to the 2^{nd} excited state. This is confirmed by applying a lower measurement pulse and observing population above the 1^{st} excited state. The two-photon frequency ν_{02} is lower than ν_{01} which is consistent with a negative anharmonicity $\nu_{12} < \nu_{01}$ and implies an anharmonicity of $\beta/2\pi = 22$ MHz since $\beta/2\pi = \nu_{01} - \nu_{12} = 2\left(\nu_{10} - \nu_{20}/2\right)$. More multi-photon transitions can be seen by applying even higher amplitudes. The qubit can be resonant with TLS's that are attributed to defects in the oxide of the Josephson junction [51]. This causes the resonance to split into two peaks which are separated in frequency by the coupling strength with the TLS. When operating the qubit, it is important to avoid these couplings since they induce decoherence and reduce measurement visibility and gate fidelity. In order to observe the TLS a measurement of tunneling probability as a function of frequency and flux is performed (see Fig. 2.5b) . TLS's can be observed by the avoided level crossing seen in the measurement which splits the resonance. The frequency monotonically decreases with flux since the potential well is getting shallower. Resonance frequency closely follows $\nu_{01} \propto (a + b\Phi_{ext} + c\Phi_{ext}^2)^{1/4}$ as expected from theory. To avoid coupling to the TLS's, the qubit is operated at ν_{01} which is at least Ω_{max} away from the closest avoided-level crossing, where Ω_{max} is the maximal Rabi frequency in our experiment.

2.4 Transmon Measurement Setup

The transmon sample that was used, based on epitaxial tunnel junctions and interdigitated capacitors, is described in [37]. The measurement setup is shown in Fig. 2.6. As mentioned in Sec. 1.3.4, the qubit is measured in the dispersive regime by measuring a shift in the resonance frequency of the coupled res-

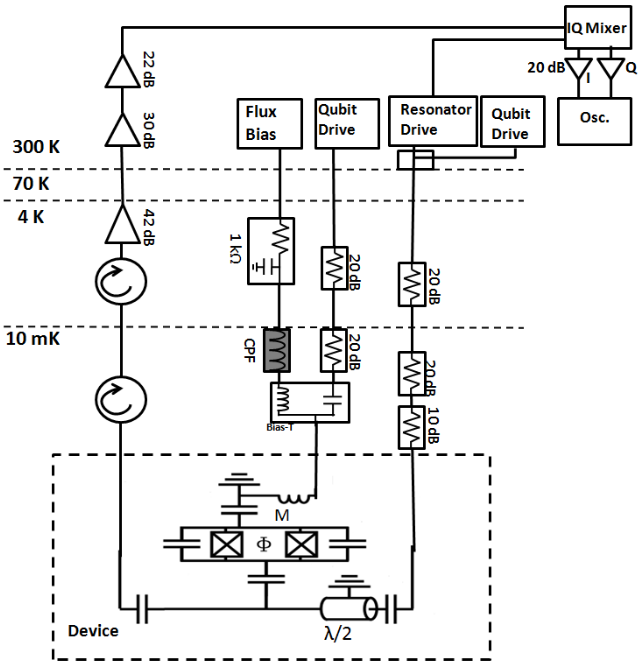

Fig. 2.6: Schematics of the measurement set-up for the transmon qubit

onator. To achieve that, the following method was used: a microwave drive resonant with the cavity is generated at the Anritsu LO. The output drive is split, one channel goes to the resonator and the other to an IQ mixer for reasons that will be explained later . After preparing the qubit state, the resonator is interogated using the microwave drive. The signal at the output of the resonator is amplified to increase SNR, first by a low noise cryogenic HEMT amplifier[7] at 4 K and then by two other low-noise amplifiers at room temperature[8]. SNR for measurement in the dispersive regime is given by ([62], [35] - Sec. 3.4.5):

$$SNR = \frac{\hbar\omega_r}{K_B T_N} \frac{\kappa T_1 \bar{n} \chi^2}{\kappa^2/4 + \chi^2} \tag{2.4.1}$$

---

[7] LNF-LNC4_8A; 42 dB amplification; Noise Temperature $T_N = 2$ K

[8] LNF-LNR4_14A, 31 dB, Noise Figure NF = 0.7 dB and B&Z 2-8 GHz, 22 dB

where $\kappa/2\pi$ is the cavity linewidth, $\bar{n}$ is the average photon number in the cavity and T_N is the noise temperature of the cryogenic amplifier. Substituting the parameters written in [37] for $\Delta = 1$ GHz which is least susceptible to flux noise, and using the linewidth measured in Sec. 3.3, the calculated SNR is $\simeq 7$. In order to gain information about both phase and amplitude of the envelope, I, Q values are extracted. This is done using an IQ mixer (see Sec. 2.2), this time used in the opposite way. The signal generated to interogate the resonator was split in the output of the Anritsu LO. The other split signal is inserted to the IQ mixer detuned by f_{IF} =40 MHz from the resonator drive. The resonator output is mixed in the IQ mixer with the detuned signal and both signal quadratures are thus extracted: $I(t) = A(t)\cos(\omega_{IF}t + \phi(t))$; $Q(t) = A(t)\sin(\omega_{IF}t + \phi(t))$. In principle f_{IF} can be set to zero but this makes the I, Q values susceptible to $1/f$ noise, voltage offsets and drifts. $I(t)$ and $Q(t)$ are amplified[9], digitized in a Lecroy Waverunner 44Xi oscilloscope, averaged to increase SNR and sent to a computer. The quadratures are then numerically rotated:

$$R(t) = \begin{pmatrix} \cos(\omega_{IF}t) & \sin(\omega_{IF}t) \\ -\sin(\omega_{IF}t) & \cos(\omega_{IF}t) \end{pmatrix}$$

the signal's amplitude $A(t) = \sqrt{I(t)^2 + Q(t)^2}$ and phase $\phi(t) = \arctan(Q(t)/I(t))$ are then calculated. $R(t)$ can be changed to correct for small imbalances and cross-talk between the mixer's IQ channels. The qubit resonance frequency can be tuned by a bias current as depicted in Fig. 2.6. The qubit can be manipulated by microwave pulses entering through either the flux bias channel or the resonator channel via a microwave combiner.

---

[9] Minicircuits GALI 3+, 20 dB

CHAPTER 3

Results

3.1 Genetic Optimization

Genetic algorithm (GA) has been developed in the last 50 years by several contributors. One of its distinct developers is John Holland [63] that has laid the foundation for future developments of the algorithm. GA has applications in a variety of fields, such as Bioinformatics, Electronic circuit design, Economics, and many others. GA was also used for evolution of robot locomotive learning [64] and recently for identifying analytical laws underlying physical phenomena[65]. GA, as the name suggests, mimics the process of natural evolution. It is used mainly to generate solutions to optimization and search problems. The wide variety of applications are possible because of the generality and relative simplicity of the algorithm. In GA, a population of strings named chromosomes or the genotype of the genome, which encode cadidate solutions to an optimization problem, are evolved towards better solutions. Initially a group of individual solutions are randomly generated to form an initial population. During each successive generation, a proportion of the existing population is selected to breed a new generation. Individual solutions are selected through a fitness-based process measured by a fitness function, where the fitter solutions are typically more likely to be selected. The selected solutions, named “parents” are breeded to create “child” solutions which typically share the characteristics of the parents. Some of the population can be mutated which meaning that a part of the chromosome is randomly mutated so that even if the solution population converges to a local minima of optimal solutions, there is still a random part that can search for other minimas.

3.1.1 Methodology

The phase qubit's anharmonicity makes it possible to excite specific levels and superpositions since each transition frequency is different. However, fourier broadening of the drive and power broadening of the transition frequency require the excitation pulses to be longer and lower in amplitude. Consequently, decoherence has a larger effect on the prepared state, resulting in lower fidelity of the prepared states. This calls for an optimization of the excitation pulses which can be achieved by a genetic algorithm. The optimization can be used to prepare single level states and superpositions of two or more states with controllable probability amplitudes using feedback from the experiment as will be later shown. The method is as follows:

(a) Initialization: N_C number of pulse sequences (chromosomes), decomposed into N_t I and Q values for each nanosecond are randomly selected by a computer. The I and Q values have a maximal amplitude Ω_{max}. The sequences are then fed to the DAC and occupation probabilities are measured.

(b) Fitness function: using the measured occupation probabilities, the population overlap given by: $\chi = \sqrt{\vec{P}_{ideal}} \cdot \sqrt{\vec{P}_{meas}}$ is calculated. Each chromosome has a population overlap associated with it. The chromosomes are then sorted in order of decreasing χ.

(c) Breeding: the first N_a chromosomes are kept as they are. The next N_a chromosomes are replaced by a combination of the upper N_a+1

chromosomes given by: $\vec{C}_{N_a+k} = \vec{B}(C_k, C_{k+1}) + \vec{\epsilon}$ where $\vec{B}(C_k, C_{k+1})$ is a breeding function and $\vec{\epsilon}$ is a set of randomly generated sequence with a small amplitude ϵ_{max}, the mutation. The bottom $N_c - 2N_a$ chromosomes are randomly generated as in (a).

(d) The bottom $N_c - N_a$ chromosomes are measured. The chromosomes are ordered with decreasing χ. Those with a higher χ than the top chromosome (C_1) are measured again N_{rep} times to reduce the uncertainty in χ. The average of χ, $\langle\chi\rangle$ is calculated out of the N_{rep} measurements and the chromosome is positioned by the value of $\langle\chi\rangle$ inside the ordered population. Step (c) is repeated.

The breeding function $\vec{B}(C_k, C_{k+1})$ can be one of many other possible alternatives. Three different functions were experimented with. The function that was used in the work presented here randomly chooses I, Q values from each parent every nanosecond, thus creating a random mix between the two parents. Another example for a function is one that averages the amplitudes of the two parents.

The fitness function has also a range of possiblities. The function we used, χ, is biased towards minimizing the population of undesirable levels and less sensitive to the distribution between the target levels. This is important for Wigner distribution measurements described in the next section since unwanted excitation at higher levels can cause a dispersion in the Wigner distribution when more than two levels are involved. Other functions can bias to optimization differently and one could choose the function which is the most suitable.

When implementing the algorithm experimentally, there are two issues that should be addressed.

Shot Noise. The population measurements for each chromosome are repeated 900 times in the experiments done in this work. The average population values are used to determine χ. The average has a statistical uncertainty of $\sim 3\%$[59]. Consequently, chromosomes which are found to have higher χ by less than 3% might actually be below the fittest chromosome. This can interfere with the optimization process. To make sure that the χ is indeed the highest for a certain chromosome, more repetitions are performed as described in step (d). The task can become tedious if this is done for every breeded chromosome. For that reason more repetitions are done only for chromosomes that are found more fit than the other after the first 900 measurements.

Flux drifts. The flux voltage slowly drifts during the experiment. Since the optimization can run for several hours, this affects the population measurements since the qubit transition frequencies are changed. This is corrected by performing a flux sweep near the initially set flux bias every 10 minutes when the drive is set to the transition frequency. By measuring the change in the resonance peak, the flux bias is tuned. In addition, drifts in the I and Q offsets are also corrected to eliminate leakage of the microwave drive.

3.1.2 Optimization Analysis

The genetic optimization depends on several parameters: the length of the chromosome or pulse N_t, the amplitude of added noise $\vec{\epsilon}$, breeding function and fidelity measure. The stochastic nature of the algorithm and its dependance on the various parameters makes it impossible to predict the way it will converge to equilibrium. Nonetheless, by observing dozens of optimizations for various target states a number of interesting characteristics are found. First, The optimization converges more quickly and to higher χ when increasing N_t. This is expected, since there are more degrees of freedom that can be played with. However, due to decoherence, longer pulses will generate states with

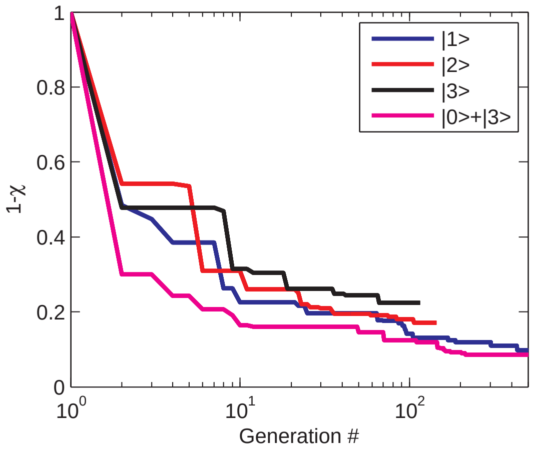

Fig. 3.1: The error $1-\chi$ as a function of generation number for various state optimizations.

lower purity. Second, the fitness function[1] increases rapidly as a function of generation number close to maximum and then converges in a logarithmic manner to the maximum value (Fig. 3.1). The fitness function was observed to saturate faster with lower noise $\vec{\epsilon}$ introduced in the system. This is reasonable since more noise causes the optimization to deviate from its course to the local minima. Consequently, when reaching high fidelity values ($\chi \gtrsim 85\%$), $\vec{\epsilon}$ is decreased manually. Since the algorithm has random initial conditions (step (a) in Sec. 3.1.1) it was found that the saturation value is not sensitive to initial conditions by repeating the optimization algorithm several times.

In order to observe the dynamics of the genome as a function of generation number, optimization data for target state $1/\sqrt{2}\,(|0\rangle + |4\rangle)$ (Fig. 3.2) including the set of 20 top chromosomes is plotted. As can be seen, the best configuration cascades down to the lower chromosomes, thus making similar descendants that cause the algorithm to converge more efficiently. The noise $\vec{\epsilon}$ was decreasesd manually by an order of magnitude from generation 41 onwards to speed up the convergence process and it is clearly observed that the diver-

---

[1] In the case of optimization of single levels $|\Psi\rangle = |l\rangle$ we use $\chi = P_l$

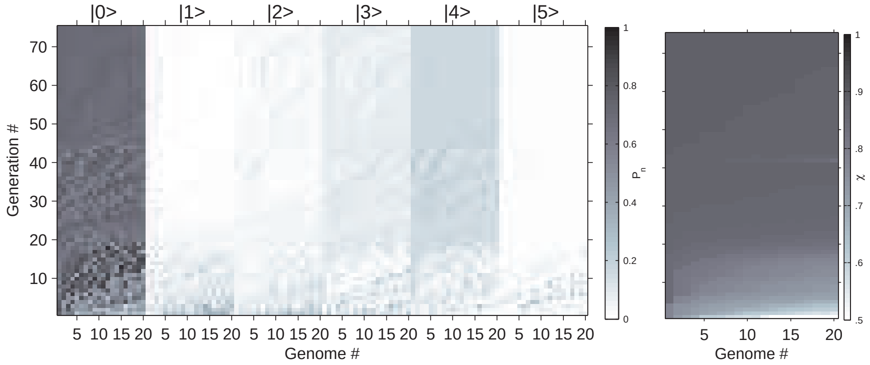

Fig. 3.2: State populations evolution of the $|0\rangle + |4\rangle$ state optimization. Left: Level population P_n vs. iteration number and level number n for the 20 best chromosomes. The chromosome length is $Nt = 40$. Right: calculated population overlap.

sity of the following generations decreases. However, the convergence can be to a local minima rather than a global minima. If the convergence process occurs too quickly it can prevent the algorithm from spreading out to search for other minimas which can be higher in fitness. This effect of premature convergence is one of the most frequent difficulties that arise when applying GA's to complex problems and is associated to loss of diversity. The results presented thus far indicate that this may be the case in our algorithm. As seen from Fig. 3.2, keeping the noise level constant throughout the algorithm may slow the convergence process. Further work to improve the algorithm can be done by using crowding techniques [66] that allow the algorithm to converge to multiple, highly fit and significantly different solutions or alternatively to slow down convergence.

3.1.3 Pulse Analysis

The algorithm uses measured occupation probabilities as the measure for the fitness function. This is in fact the only feedback needed from the experimental system to perform the optimization. To ensure that the measured occupation

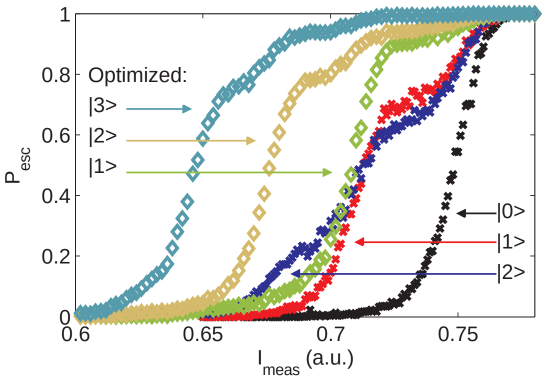

Fig. 3.3: Optimized vs. non-optimized escape curves. Escape curves, measured immediately after state preparation in the case of non-optimized states (right) and genetically optimized states (left) at small anharmonicity ($\beta/2\pi = 22MHz$). In manually prepared second excited state a long pulse is used, resonant with the two photon transition to minimize excitation of higher levels. This results in only 25% of the population in this level. Preparation of higher excited states results in even a lower fidelity.

probabilities are correct, the escape curve (sec. 2.3.2) of each of the single level optimized pulses up to level $|3\rangle$ is measured independently as shown in Fig. 3.3. These are compared with escape curves of manually prepared states. All measurements were done in the low anharmonicity regime ($\beta/2\pi = 22$ MHz) using a sequence length of 20 ns, 20 ns and 12 ns for the first, second and third excited states, respectively. The escape curves are consistent with the measured occupation probabilities of each pulse in the optimization algorithm.

In order to study the structure of the optimized pulses, the fittest chromosome in each target state was convolved with the DAC impulse response (Sec. 2.2) and then fourier-transformed as shown in Fig. 3.4. One can observe the asymmetry of the spectrum due to the interference of several frequencies in the pulse. This is necessary to reduce the amplitude in transition frequencies that can excite the population to unwanted levels. For example, in the red curve of the single level target states there is a minima on f_{12} to eliminate the excitation from the first to the second excited levels and this pattern repeats

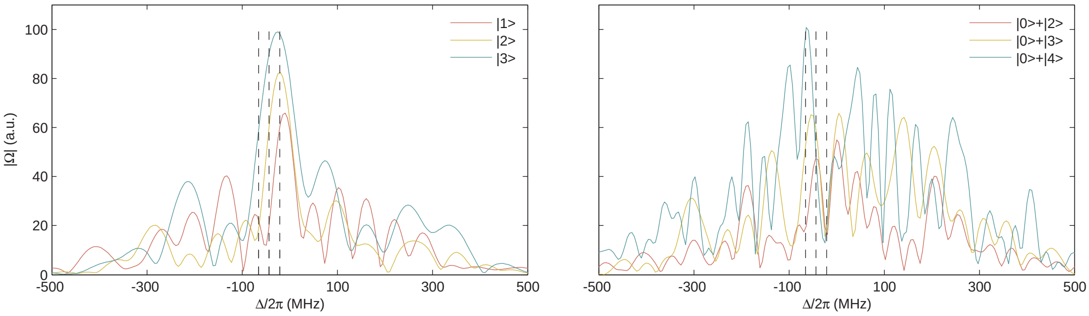

Fig. 3.4: Fourier transform amplitude of the various optimization pulses. The dashed lines represent transition frequencies f_{01}, f_{12}, f_{23} from right to left. Anharmonicity is $\beta = 22$ MHz. Left: single level target states. Right: Superposition target states.

for the other two pulses. In the yellow curve, the ratio between f_{01} and f_{12} is close to $\sqrt{2}$ which is similar to the SU(2) generator of a rotation around x treating the first three levels as an effective spin-1 particle [5]. A similar structure appears in the green curve as well. The superposition optimization show a more complex spectrum which involves more frequencies. Nevertheless, one can observe that the pulses utilize the effect of two-photon transition to create the required state. In the red curve an expected minima appears on f_{01} to eliminate population in level $|1\rangle$ while a maxima appears on f_{12} to excite the unwanted population from $|1\rangle$ to $|2\rangle$. The spectrum has significant amplitude on the two-photon transition frequency f_{02}, between f_{01} and f_{12} to excite population directly from the ground state. The other pulses are of similar form having minimas on f_{01} and utilizing two photon transitions to level $|3\rangle$ and $|4\rangle$.

3.2 Wigner Tomography in an Anharmonic Oscillator

3.2.1 The Wigner Function

The Wigner quasiprobability distribution was first introduced by Wigner in 1932 to give higher order quantum corrections for classical mechanics[67]. The function is used to link the wave function of a quantum state to a probability distribution in phase space. A classical particle has a definite position and momentum and hence is represented by a point in phase space. For a collection (ensemble) of particles, the probability of finding a particle at a certain position in phase space is given by a probability distribution. This does not hold in quantum mechanics due to the uncertainty principle. The Wigner function serves in this case as a quasiprobability distribution for a quantum mechanical state. As the name implies, the function does not possess all the properties of a probability distribution. For instance, the Wigner function can be negative in certain areas in phase-space which is an indication for the quantum properties of a state. Effects such as superposition and interference between two quantum states are easily seen in the Wigner representation. In the general case which includes mixed states the function is defined as:

$$W(x,p) = \frac{1}{\pi\hbar} \int\limits_{-\infty}^{\infty} \langle x+y|\hat{\rho}|x-y\rangle \, e^{-2ipy/\hbar} dy \tag{3.2.1}$$

where x, p can be any conjugate variables.

It is instructive to observe the Wigner function of Fock states and coherent states (Fig 3.5). The vacuum state of the harmonic oscillator is, as expected, a two dimensional gaussian function around the origin. The first excited state

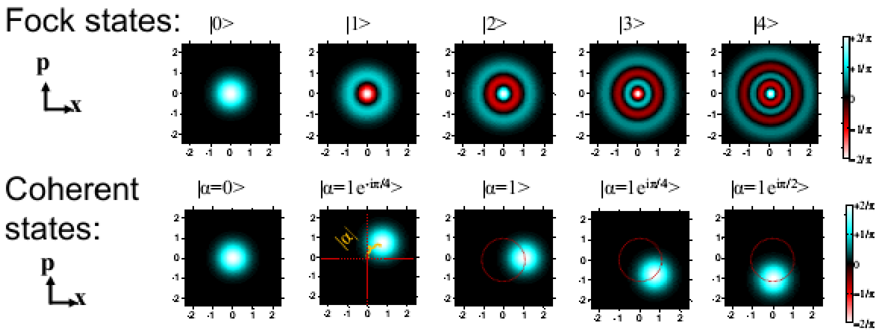

Fig. 3.5: Wigner distributions of Fock states and coherent states in a harmonic oscillator.

is negative at the origin which shows its non-classical character. The quasi-classical nature of a coherent state is indicated in Fig. 3.2 by the gaussian which is located around a certain phase space point where the uncertainty in position and momentum is represented by the width of the gaussian. The gaussian rotates around the origin, similar to a classical particle.

The Wigner distribution is especially useful when dealing with systems with continuous degrees of freedom, such as atoms in molecules in which wavepackets often form and their dynamics are best described in phase-space. Since the Wigner distribution holds all of the information about a state, it can be transformed into a density matrix representation of a quantum state, thus providing an alternative method of state tomography measurement[1, 68]. Both statements form the motivation for the experiment described in this chapter.

3.2.2 Wigner Tomography in the Josephson Phase Qubit

The Wigner function has been measured in various experiments involving harmonic [69, 70] and anharmonic atomic and molecular systems[71]. In the experiment described in this chapter, the Wigner distribution was measured in the phase qubit which is an anharmonic quantum oscillator. As described previously, it is not possible to measure the Wigner function directly in the charge-phase basis. In order to overcome this difficulty, a theorem by Royer relating the Wigner distribution to the expectation value of the parity operator[72] is used. The expectation value is calculated from the measured occupation probabilities using harmonic oscillator eigenstates and is given by :

$$W(\alpha) = (2/\pi) \sum_{n} (-1)^n \, P_n(\alpha) \tag{3.2.2}$$

where α is a complex number representing the phase space coordinate and $P_n(\alpha)$ is the n-th level occupation probability after a displacement operation $D\,(\alpha)$. Eq. 3.2 was used to measure the Wigner function of a superconducting resonator through a Josephson phase qubit[73]. Using Eq. 3.2 for Wigner tomography in the phase qubit poses several challenges since the phase qubit is anharmonic: first, in order to approximate a displacement operation, one has to apply a pulse which is resonant with all transition in the measured subspace. Second, during the displacement (tomography) pulse, the phase of each level ϕ_n in the rotating frame advances in an increasing rate with n, causing wavepackets to disperse in phase space. For example, in a cubic potential this rate is given by $\dot{\phi}_n \approx \beta n(n-1)/2$, where $\beta = 2\pi\,(f_{10} - f_{21})$ is the anharmonicity and $n = 0, 1, 2, ...$. Third, the eigenstates of the anharmonic oscillator are not parity eigenstates. It is found that the three difficulties can be partically overcome by applying short (1.6 ns) gaussian tomography pulses and biasing the phase qubit in the low anharmonicity regime ($\beta = 22$ MHz).

3.2.2.1 Tomogrpahy Pulse The displacement phase and amplitude are controlled by the relation $\alpha = -\frac{1}{2}\int \Omega(t)dt$ where $\Omega(t)$ is the time-dependant short gaussian Rabi amplitude. Fig. 3.3 shows the tomography pulse in the fre-

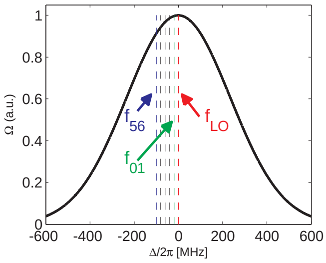

Fig. 3.6: Tomography pulse in the frequency domain. Red dashed line is the local oscillator frequency and colored dashed lines represent to the first five transitions. The envelope is a normalized gaussian corresponding to the 1.6 ns FWHM gaussian tomography pulse. The first five transitions vary in the range of 10% in amplitude.

quency domain. The first five transitions vary in amplitude by 10% which is in agreement with the systematic errors in data and simulation as will be discussed in section 3.2.5. More transitions can be covered in principle by shifting the local oscillator lower in frequency. A harmonic displacement can be well approximated in an anharmonic system under the condition: $\beta T \left|\alpha\right| m^2/4 \ll 1$ where $|\alpha|$ is the displacement amplitude, T the tomography pulse length and m is the maximal occupied level after the displacement (see Sec. 3.2.5). This condition poses a hard limit on the measurement which seemingly renders the protocol to be impossible to implement in our system. However, it was checked by simulations that under the experimental parameters the approximation holds for measurements of states which are excited up to the $5-th$ level. There are two reasons for that: first, while the phases of the displaced state are sensitive to the above condition, the parity value remains insensitive for larger displacements. Second, the lowest five states have a well defined parity to within 1% and that these are the main contributors to the expectation value of the parity operator.

3.2.2.2 Population Measurements Population measurements were done with a novel measurement pulse shape (see Fig. 3.3) . As mentioned in Sec. 2.3.2,

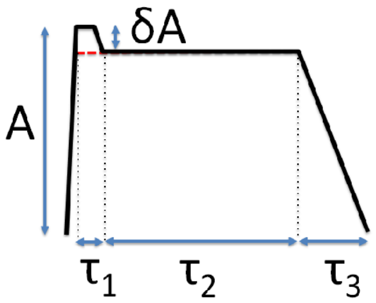

Fig. 3.7: Measurement pulse shape for Wigner tomography experiment

the measurement pulse decays slowly in order to eliminate retrapping in the qubit potential well. In the low anharmonicity regime, the length and decay of the pulse have to be sufficiently long since the qubit well is deeper (~ 25 levels). In the experiment $\tau_2 = 25$ ns and $\tau_3 = 15$ ns were used. Because the length of the pulse is comparable to the decay time of the qubit (see for reference Sec. 2.3), during the pulse population from higher levels decays and tunnels out. This results in a distortion of the Wigner measurement. To reduce this effect the pulse is slightly higher by an amount δA ($\sim 10\%$ of A) at the begininng for a duration $\tau_1 = 1$ ns to allow the relevant population to tunnel out and then lowered to prevent tunneling of higher excitations.

In order to verify that the tomography pulse produces an approximate coherent state, state occupations were measured after a tomography pulse and compared to a calculation in the harmonic case with the poissonian distribution: $P(\alpha, n) = (1/n!) \exp(-|\alpha|^2) |\alpha|^{2n}$ (see Fig. 3.4) . The data fits well to theory although the populations are slightly biased to the lower levels. This is expected since the displacement in the anharmonic system slightly decreases in amplitude of the higher transition frequencies as discussed earlier.

3.2.2.3 Density Matrix Extraction The density matrix is extracted using the harmonic oscillator basis [73] from 200 tomography points randomly picked

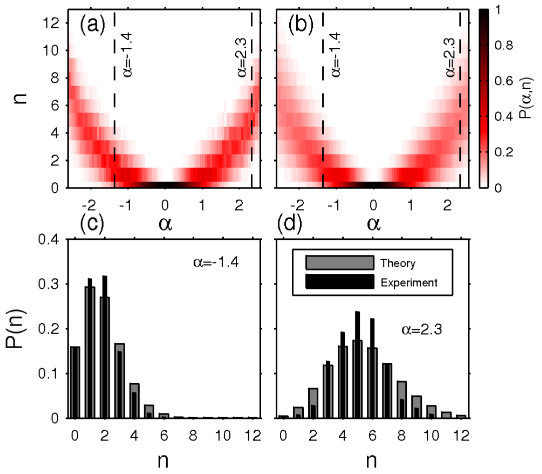

Fig. 3.8: Occupation probabilities following a displacement operation. *Top:* (a) Calculated state occupation probabilities in the harmonic case as a function of displacement amplitude $|\alpha|$. (b) Measured occupation probabilities as a function of displacement amplitude $|\alpha|$. *Bottom:* Calculated and measured probabilities in the case of $|\alpha| = 1.4$ (c) and $|\alpha| = 2.3$ (d).

inside a circle with radius $|\alpha| < 2$ in phase space while restricting the density matrix to a 6×6 subspace. The tomography pulse induces a rotation of the measured state ($\Gamma(t)$, see Sec. 3.2.5) which affects the off-diagonal elements in the density matrix. To get more accurate phases, one can apply an inverse propagator on the density matrix $U = \exp(-iH_0\Delta t/\hbar)$, where H_0 is the drive-free Hamiltonian and Δt is the effective pulse length for the rotation.

One of the important motivations of this experiment is the use of Wigner tomography as a state tomography (ST) technique. The protocol described above requires a relatively simple calibration which mainly involves measuring the tunneling curves of the different levels as described in Sec. 2.3.2. Since the density matrix of the state can be extracted from the Wigner distribution, this can be seen as an alternative ST measurement method. ST for multi-level states requires a long calibration process of the different rotations in the SU(n) Hilbert space [12]. In Sec. 3.2.5, the threshold for the number of tomogra-

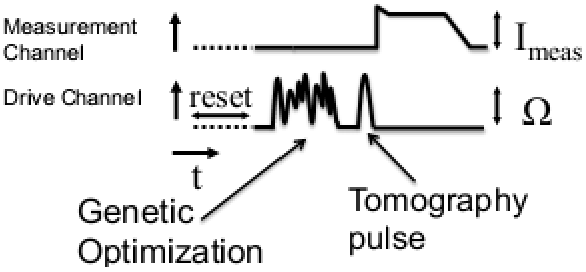

Fig. 3.9: Experimental sequence for wigner distribution measurements of Fock state superpositions

n	$P(\|0\rangle)$	$P(\|1\rangle)$	$P(\|2\rangle)$	$P(\|3\rangle)$	$P(\|4\rangle)$	$P(\|5\rangle)$	τ (ns)	χ (%)
1	0.52	0.47	0.01	0	0	0	15	99.8
2	0.69	0.05	0.24	0.02	0	0	30	93.4
3	0.58	0.03	0.11	0.27	0.01	0	25	90.5
4	0.70	0.01	0.03	0.07	0.17	0.02	40	88

Table 3.1: Results of the optimization algorithm.

phy measurements required to extract the density matrix and measurement error are analyzed, rendering Wigner tomography as an efficient and reliable ST measurement method.

3.2.3 Wigner Tomography of Fock State Superpositions

To verify the above technique, Fock state superpositions of the form $|\Psi_l\rangle = \frac{1}{\sqrt{2}}\left(|0\rangle + e^{i\delta}|l\rangle\right)$ were measured. These superpositions were chosen since they have a lucid geometry in phase-space and having only one degree of freedom, the phase δ, they do not disperse but simply rotate. States were prepared by a genetic optimization by (see Sec. 3.1.1 and sequence in Fig. 3.9) with relatively long pulses, sacrificing state purity for fidelity and run-time. Optimization results are depicted in table 1 . As mentioned in Sec. 3.1.1, the algorithm can only be applied to level occupation probabilities. Consequently, each superposition was prepared with an arbitrary δ.

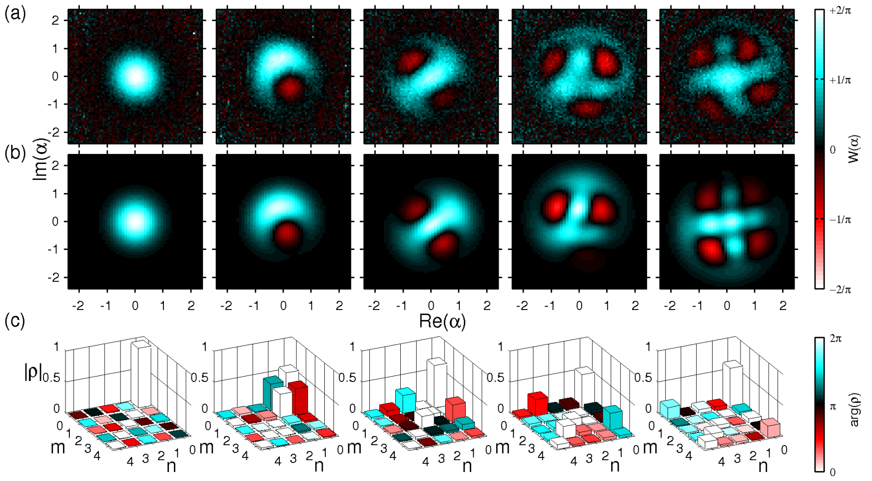

Fig. 3.10: Superposition of Fock-type states. (a) Wigner tomography of genetically optimized superposition of Fock-type states and (b) calculated Wigner distributions of these states, using level occupations from table 1 and phases of the extracted density matrices. (c) Extracted density matrices from the measurements shown in (a).

The Wigner distributions of the various states are shown in Fig. 3.10 The measured distributions for the ground state and $|\Psi_l\rangle$are shown (3.10a) and compared with the calculated distributions using the measured occupation probabilities in table 1 (Fig 3.10b). The extracted density matrices from the distribution measurement are presented in Fig. 3.10c. The diagonal elements are in agreement with the measured occupation probabilities in table 1. However, simulation results show that the off-diagonal elements deviate increasingly for $n > 2$. The causes for the deviation are decay and decoherence of the higher excited states. This can be improved by using higher coherence samples. Superpositions of 3 or more levels can be measured, although the phases will disperse during the tomography pulse. Nonetheless, these can be corrected using the time-reversed propagator of the bare system.

3.2.4 Wavepacket Dynamics Measurements

As mentioned in Sec. 3.2.1, Wigner tomography is especially useful for measuring wavepacket dynamics in phase-space. These include effects such as autoresonance and phase-locking between the system and the drive that can take place within certain conditions [74]. Phase-locking to the drive may occur when the system is driven with a frequency chirp, such that the system's oscillation frequency follows that of the drive. This phenomenon occurs above an amplitude threshold, which depends on the chirp-rate and anharmonicity. In a system with negative anharmonicity ($f_{01} > f_{12}$), a negative frequency-chirped drive ($\dot{f}_{drive} < 0$) can cause phase-locking at sufficiently large amplitudes, depending on the chirp rate and anharmonicity. While the transition between ladder climbing and autoresonance has been studied by Shalibo et al in the Josephson phase qubit [75], phase-locking was not shown experimentally. The measurement of the Wigner distribution described in this section opens up the possibility to measure this effect directly for the first time. To measure this effect, the system was initiated in the ground state and a negative frequency chirp was applied with a drive amplitude above the phase-locking threshold and a final frequency centered close to the transition frequency f_{23} (see Fig. 3.11). The chirp's temporal length and bandwidth $|f_{fin} - f_{in}|$ are chosen to be short (20 ns) and large (600 MHz) respectively, in order to have a broad excitation of states and for the excitation to be adiabatic [75] .

Fig.3.12 shows tomography measurements at different times during the chirp (Fig. 3.12a) and after the drive has been turned off (Fig. 3.12b). The axes of each time frame were rotated to fit the rotating frame of the drive. During the chirp, wavepacket formation can be observed that gradually acquires a constant phase as the drive crosses the linear resonance ($f = f_{01}$). This occurs, as expected, at $t = 16$ ns and the shape of the wavepacket be-

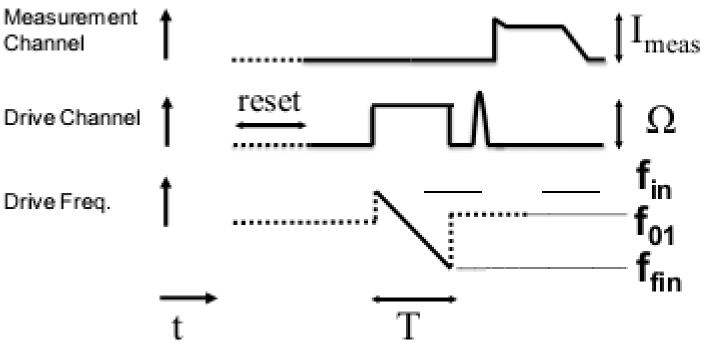

Fig. 3.11: Experimental sequence for wavepacket dynamics measurement

comes crescent-like. After the drive is turned off, phase-locking is lost and the wavepacket disperses. After 35 and 50 ns, one can still observe coherences between the states indicated by the negative areas in the Wigner distribution. To study decoherence dynamics in the system, the state purity which is given by: $\wp = \pi \int d\vec{\alpha}\, |W(\vec{\alpha})|^2$[76] is calculated for each time frame. Experimental results are shown in Fig. 3.13 by the red circles and compared with simulation (solid line) . The purity remains close to 1 during the chirp and decays after the chirp ends due to decoherence. The purity reaches a minimum and then increases exponentially as it returns to the ground state, consistent with simulation using experimental decoherence parameters T_1 and T_2.

3.2.5 Errors and Discussion

In order to calculate the errors in the extracted density matrix, several numerical simulations were performed ([59], Sec. 3.4.4.1, 3.4.4.2) . There are two types of errors: systematic errors and statistical uncertainty. The systematic errors are due to the limitations of the experimental system which are the finite anharmonicity and decoherence. Statistical uncertainty is present in all probabilistic measurements and was compared with the state tomography technique

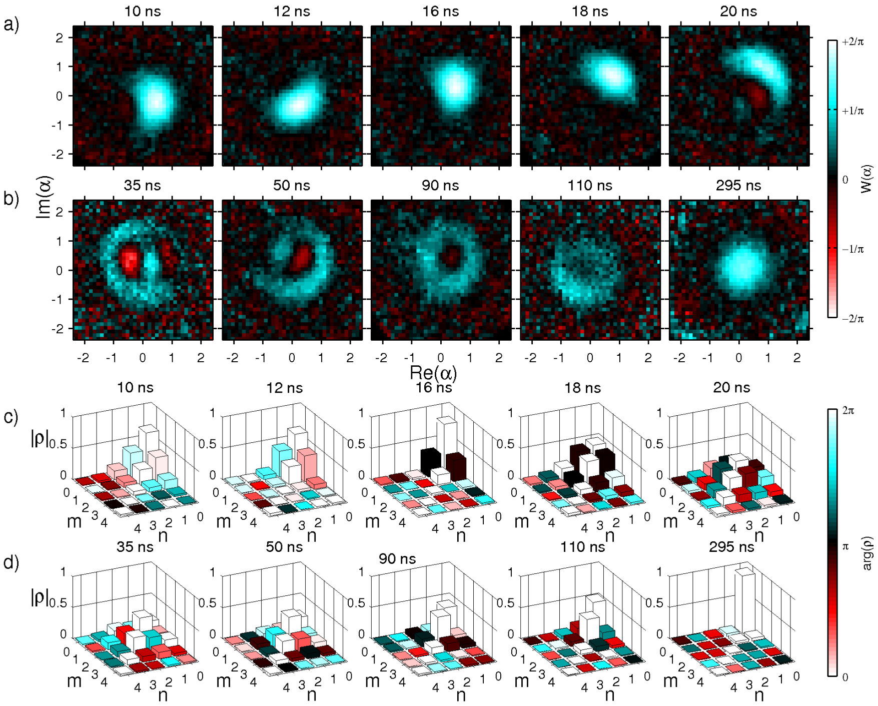

Fig. 3.12: Dynamics of a phase-locked wave-packet. (a) Wigner tomography during a chirp ($T = 20\,\mathrm{ns}$, $\Omega/2\pi = 66\,\mathrm{MHz}$, $f_{in} - f_{01} = 320\,\mathrm{MHz}$, $f_{fin} - f_{01} = -50\,\mathrm{MHz}$), and (b) during drive-free evolution. (c) and (d) show the extracted density matrices for (a) and (b) respectively.

.

Systematic errors were studied by simulating the experimental tomography pulse applied to an anharmonic system initialized with a pure state. In the rotating wave approximation the tomography pulse is represented by the propagator: $\mathrm{U}(t) = \exp\left(i\frac{\delta t}{2}\left[\left(\Omega(t)a^\dagger + \Omega(t)^* a\right) + \beta a^\dagger a(a^\dagger a - 1)\right]\right)$, where δt is the time step in the simulation and $\Omega(t)$ is the time dependent drive envelope amplitude. Assuming small anharmonicity with a constant drive amplitude Ω of total duration T, $U(t)$ can be approximated by the Zassenhaus formula [77] to $U \approx D(\alpha)\Gamma(t)\exp(-i\frac{T\beta}{4}[\left(\alpha a^\dagger - \alpha^* a\right), a^\dagger a(a^\dagger a - 1)])$ where $D(\alpha)$ is the displacement operator, $\Gamma(t)$ is a global phase acquired during the tomography pulse and $\alpha \equiv i\Omega T$. The third term can be considered negligible in the

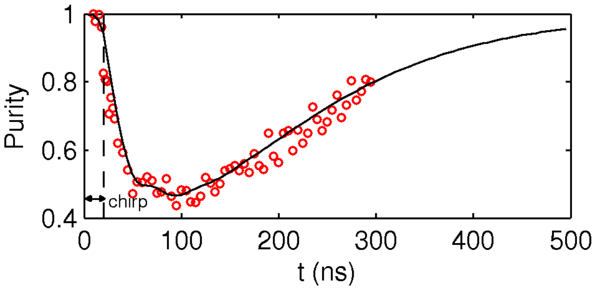

Fig. 3.13: State purity. Extracted state purity $\wp$ from experiments (red circles) and simulation (solid line) during chirp and decay. The simulation includes the effect of the decay and dephasing and agrees with the measured decay time of $T_1 = 120\,$ns.

limit $|\alpha|T\beta m^2/4 \ll 1$, where m is the maximal occupied state. Placing the experimental parameters, the third term can be neglected only for $|\alpha| \ll 1$. However, the error in the Wigner distribution, obtained from the state populations after the pulse is negligible even for $\alpha \approx 2$, as seen from simulations (see sec. 3.2.2 for explanation). Simulations show that the error in standard fidelity $\mathcal{F} = Tr\sqrt{\sqrt{\rho^F}\rho^I\sqrt{\rho^F}}$ of the extracted density matrix of the experimental distributions relative to that of the ideal distribution increases exponentially with anharmonicity and maximal level, as expected. The fidelity is sensitive to decoherence level which is more pronounced as the maximal level is increased since the decay and dephasing times are shorter for higher levels. Maximal errors with current experimental parameters are 17% for the amplitude of each term in the density matrix and $\sim 1.5\%$ for the phase. Nevertheless, for currently available samples having $T_1 > 600$ ns and correspondingly longer T_2, the errors due to decoherence can be substantially reduced; In this case, the errors become smaller than 0.1 in all measured superpositions described above.

To quantify the statistical errors of both state tomography technique (ST) and the Wigner distribution measurement, simulations of the both techniques using generated binomially distributed random numbers that represent tunneling events were done. The fidelity error of both techniques from the original state was then calculated. It was found that while ST needs a smaller amount of repeated measurements by a factor of eight for superpositions of two Fock states, in states comprising a superposition of five levels the amount of measurements were similar. This is reasonable since ST is done using the energy basis which is more suitable for single level and two level superpositions but when trying to deterimine the state of multi-level superpositions that are partially localized in phase space, both phase space basis and energy basis can be used efficiently.

3.3 Transmon Measurements

The first step in characterising the transmon qubit was a spectroscopic measurement to determine the cavity frequency. An incoherent measurement tone of length τ ($\tau = 6\mu s$) was applied to the cavity and a window of 200 ns containing the transmitted signal from the cavity was averaged 1000 times for each measurement in the oscilloscope. Averaging improved SNR from ~0.1 to ~4. Cavity spectroscopy is shown in Fig. 3.14. The resonance peak is a Lorentzian with a linewidth of $\kappa = 7.5$ MHz corresponding to $Q \simeq 1100$. In order to observe the qubit resonance, the average photon number in the cavity has to be less then $\bar{n} \simeq 20$. Higher powers would result in a larger stark shift and an inhomogenous broadening of the qubit resonance due to fluctuations of photon number of the order $\sqrt{n}$ which translate into fluctuations in the qubit frequency ([35], Sec. 8.2.1). Using the steady state formula for photon number in the cavity: $\bar{n} = P_{in}/\hbar\omega_r\kappa$ where P_{in} is the input power, the maximum power that can be inserted is $P_{in_{max}} \simeq 10^{-15}$ W. The microwave drive power in the DAC chain output after 20 dB attenuation is -60 dBm. The combiner provides another 9 dB attenuation. Adding the 50 dB of cold attenuation and

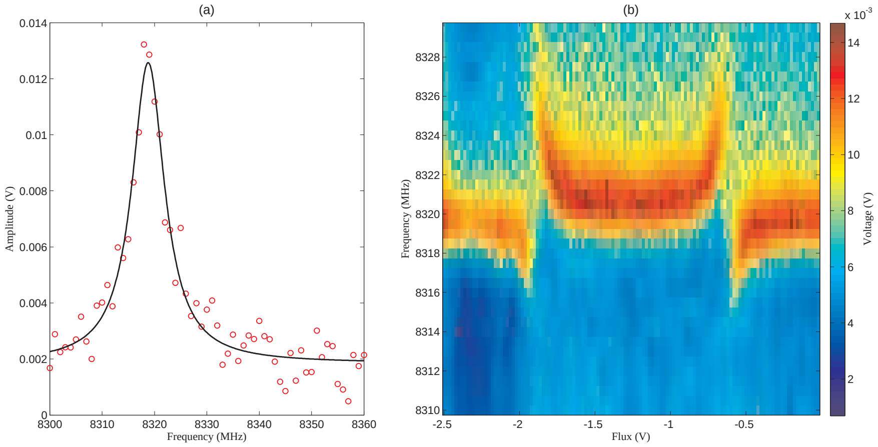

Fig. 3.14: Transmon measurements. (a) Resonance curve of the coupled resonator. (b) Amplitude of resonator output as a function of frequency and flux bias.

5 dB of cable attenuation (Sec. Fig. 2.6) resonator input power is $P_{in} = -124$ dBm corresponding to $\bar{n} \backsimeq 8$ which is sufficiently low. As mentioned in [37], the designed vacuum rabi frequency is $g/2\pi = 85$ MHz. Thus, when the qubit is tuned by the flux bias to have its first transition frequency degenerate with the cavity there should be an avoided level crossing with a splitting g. Fig. 3.14b shows a measurement of the transmitted amplitude from the cavity as a function of microwave frequency and flux bias. As can be seen, there is a vacuum Rabi mode splitting but with a much weaker coupling of $g/2\pi = 2$ MHz. This pattern is periodic and repeats in positive flux values. In this case, a dispersive measurement cannot be done since a dispersive shift of the resonator frequency is of the order $\chi = g^2/\Delta$. Inserting g to the calculation in Eq. 2.4.1 yields $SNR \backsimeq 10^{-5}$, five orders of magnitude lower than the SNR calculated in Sec. 2.4. Unsuccessful attempts to measure a qubit resonance have led to the conclusion that the sample is unfortunately unusable.

CHAPTER 4

Simulations

4.1 State Discrimination in the Josephson Phase Qubit

The concept of non-orthogonal state discrimination was first introduced in 1987 by Ivanovic [78]. A year later, Peres suggested that the infinite sequence of generalized measurements proposed by Ivanovic can be performed in a single step [79]. Experimental realizations of the protocol have been published on optical systems[80, 81]. The idea is described henceforth.

Suppose that a mixture of quantum systems are prepared in either state $|A\rangle$ or state$|B\rangle$. How well can the two states be discriminated one from the other? If $|A\rangle$ and $|B\rangle$ are orthogonal in a certain basis of measurement, a decisive answer can be given if a direct measurement is done in that basis. If the two states are non-orthogonal, the simplest method is a direct measurement that distinguishes $|A\rangle$ from its orthogonal state $|\bar{A}\rangle$. If $|\bar{A}\rangle$ is measured, one can be assured that the original state was not $|A\rangle$ and therefore was $|B\rangle$. One may consider a collection of systems as a stochastic sequence of states $|A\rangle$and $|B\rangle$ while the measurements are controlled and chosen between the two bases:$\{A, \bar{A}\}$,$\{B, \bar{B}\}$. An exact state retrodiction occurs when the system's state, $|A\rangle, |B\rangle$ coincides with measurement$\{B, \bar{B}\}$,$\{A, \bar{A}\}$, respectively. Consequently, an exact state differentiation is realized with probability: $P_{diff} = \frac{1}{2}|\langle\bar{A}|B\rangle|^2 = \frac{1}{2}\sin^2(\phi)$, where ϕ is a number representing the overlap: $\phi = 0$ corresponds to states which are completely overlapping and $\phi = \frac{\pi}{2}$ to orthogonal states. The factor $\frac{1}{2}$ comes from the requirement of coincidal measurement described above. In the protocol suggested by Ivanovic and Peres, by a direct measurement scheme using another quantum system as a probe system, $|P\rangle$ that is entangled to the inspected system, $|\Psi\rangle$, unambigous differentiation between the two states is possible with a higher probability than P_{diff}.

4.1.1 Measurement Protocol

It is often the case that a measurement can be done only in a specific basis in experimental systems. For example, in the Josephson phase qubit, a measurement is done in the energy basis. Consequently, when trying to distinguish between two states that are close to each other in the bloch sphere, state discrimination is the only possible protocol since another basis of measurement is not available. The protocol is useful if one attempts to reset the qubit and would like to know if the qubit is indeed in its ground state. In this section, a protocol is presented involving two coupled phase qubits, one serving as the probe and the other as the system in question.

Suppose that after reset, the qubit can be in one of the following states: $|g\rangle = |0\rangle$ or $|e\rangle = \cos(\frac{\theta_0}{2})|0\rangle + \sin(\frac{\theta_0}{2})e^{i\delta}|1\rangle$ where $\theta_0 \ll 1, \delta \ll 1$. The qubit is then coupled with coupling strength S to another qubit in its excited state that serves as a probe, thus: $|0\rangle_A \otimes |1\rangle_B$ or $\big(\cos(\frac{\theta_0}{2})|0\rangle_A + \sin(\frac{\theta_0}{2})e^{i\delta}|1\rangle_A\big) \otimes |1\rangle_B$. The coupled system is then rotated for a duration t_{swap}: $\cos(\frac{St_{swap}}{2})|01\rangle + \sin(\frac{St_{swap}}{2})|10\rangle$ or $\cos(\frac{\theta_0}{2})\Big(\cos(\frac{St_{swap}}{2})|01\rangle + \sin(\frac{St_{swap}}{2})|10\rangle\Big) + \sin(\frac{\theta_0}{2})e^{i\delta}|11\rangle$ and both qubits are measured. Observing only measurements with the qubit in the excited state, the probe state depends on the qubit's initial state. $|g\rangle$ and $|e\rangle$ in the qubit correspond to $|0\rangle$ and

$$\frac{1}{\sqrt{\sin^2\left(\frac{\theta_0}{2}\right)+\cos^2\left(\frac{\theta_0}{2}\right)\sin^2\left(\frac{St_{swap}}{2}\right)}}\left(\cos(\frac{\theta_0}{2})\sin\left(\frac{St_{swap}}{2}\right)|0\rangle+\sin(\frac{\theta_0}{2})e^{i\delta}|1\rangle\right) \tag{4.1.1}$$

in the probe. If $t_{swap} \ll \frac{1}{S}$ or alternatively $\sin^2\left(\frac{St_{swap}}{2}\right) \ll \tan^2\left(\frac{\theta_0}{2}\right)$, the probability for the probe to be in the excited state is close to 1. Thus, unambigous state discrimintation is achieved with probability $P_{discriminate} = \frac{1}{2}\left[\sin^2(\frac{St_{swap}}{2}) + \sin^2(\frac{\theta_0}{2})\right]$, the $\frac{1}{2}$ prefactor comes from the assumption that after reset the qubit can be in each state with equal probability.

4.1.2 Simulation

Simulation of the protocol with and without decoherence was done to verify that the protocol can be performed with currently available qubits. The simulation used two qubits with $C = 1.3$ pF capacitance and a coupling capacitance of $C_c = 3$ fF which are typical parameters of current qubits[24]. Qubit excitation frequency was set to 5.1 GHz yielding a coupling strength $S \simeq 5.89$ MHz.

In order to quantify the distinguishability of the two different states, visibility is defined as: $V_{SD} = P(1_{P,e}|1_{Q,e}) - P(0_{P,e}|1_{Q,e})$ where $1_{P(Q),e}$ is the event of measuring the probe (qubit) in the excited state and $0_{P,e}$ is the event of measuring the probe in the ground state when the qubit was initially in state $|e\rangle$. Ideally, if t_{swap} is infinitesimal and there is no decoherence, $P(0_{P,e}|1_{Q,e})$ is 0 and visibility is 100%. In the presence of decoherence a density matrix representation was used (see Appendix B) and visibility was calculated by: $V_{SD} = \frac{\rho_{11}-\rho_{10}}{\rho_{11}+\rho_{10}}$ where ρ_{ij} is the probability of the qubit being in state i and the probe in state j given that the initial state was $|e\rangle$. Fig. 4.1 shows simulation results. In Fig. 4.1a, visibility is calculated for different t_{swap} values. As expected from

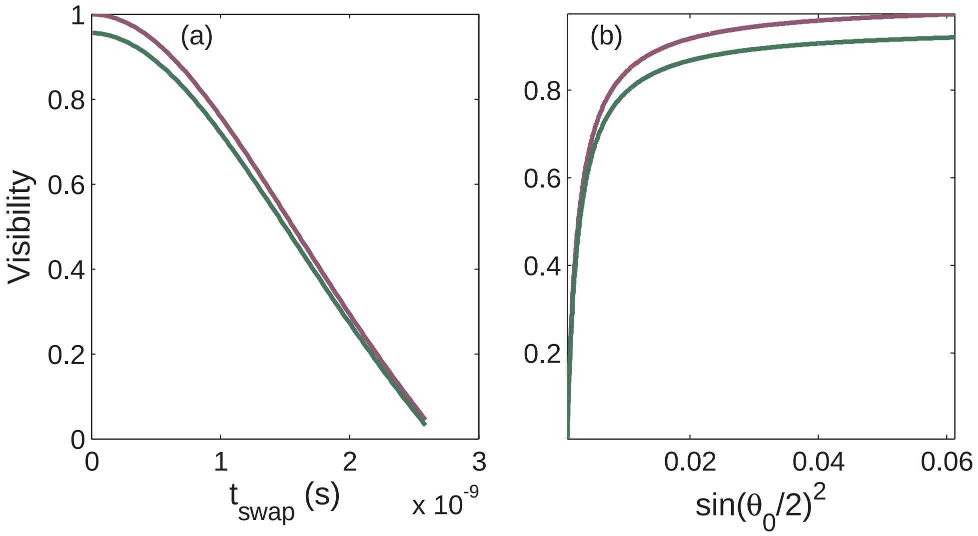

Fig. 4.1: Simulation results for state discrimination protocol: (a) Visibility dependence on t_{swap} without decoherence (purple) and with $T_1 = 300$ ns and $T_2 = 100$ ns (green); $\theta_0 = 0.1$. (b) Dependence on $\sin^2(\frac{\theta_0}{2})$ without decoherence (purple) and with $T_1 = 300$ ns and $T_2 = 100$ ns (green); $t_{swap} = 1.6$ ns.

Eq. 4.1.1, visibility decreases with increasing t_{swap}. Importantly, decoherence has a small effect on the visibility, which can be close to 100% with sufficiently short swap time. The protocol is thus feasible in current samples. In order to compare the protocol with the direct measurement, one can examine the SNR of both techniques (analysis is based on [82]). For N direct measurements, the signal is:

$$S = N_{1,e} - N_{1,g} = V_{Direct} \cdot N \sin^2\left(\frac{\theta_0}{2}\right) \tag{4.1.2}$$

where $N_{1,g}$,$N_{1,e}$ are the number of measurements of the qubit in state $|1\rangle$ given that the qubit is in state $|g\rangle$ or $|e\rangle$. The statistical noise considering the binomial distribution of the phase qubit measurement is:

$$\Delta S = \sqrt{\left(\frac{\partial S}{\partial N_e}\right)^2 \Delta N_e^2 + \left(\frac{\partial S}{\partial N_g}\right)^2 \Delta N_g^2} = \sqrt{N \sin^2\left(\frac{\theta_0}{2}\right) \cos^2\left(\frac{\theta_0}{2}\right)} \tag{4.1.3}$$

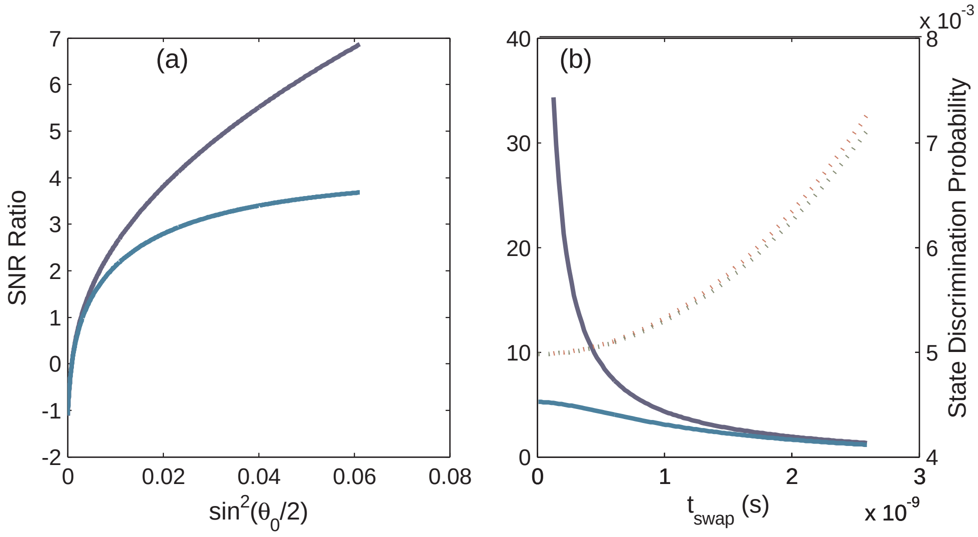

Fig. 4.2: SNR ratio and discrimination probability without decoherence ($T_1 = 300$ ns and $T_2 = 100$ ns) (purple) and with decoherence (blue) (a) SNR ratio as a function of $\sin^2(\theta_0/2)$ with t_{swap} =1.6 ns . (b) SNR ratio (solid, same as in (a)) and discrimination probability (dashed) with decoherence (green); w/o decoherence (red) as a function of t_{swap} with $\sin^2(\theta_0/2) \sim 1\%$. V_{direct}= 85%.

Hence, the SNR for a direct measurement is: $SNR_{Direct}(N) = \frac{S}{\Delta S} = V_{Direct} \cdot \sqrt{N} \tan\left(\frac{\theta_0}{2}\right) \simeq V_{Direct} \cdot \sqrt{N}\theta_0/2$. In the state-discrimination protocol, the signal is:

$$\tilde{S} = \left(\frac{N_{1,1,e}}{N_{1,0,e}+N_{1,1,e}} - \frac{N_{1,1,g}}{N_{1,0,g}+N_{1,1,g}}\right) \cdot V_{SD} \cdot N_{SD} = N \cdot \frac{1}{2}\left[\sin^2(\frac{St_{swap}}{2}) + \sin^2(\frac{\theta_0}{2})\right] \\ \times V_{SD} \cdot \frac{\sin^2(\frac{\theta_0}{2})}{\sin^2\left(\frac{\theta_0}{2}\right)+\cos^2\left(\frac{\theta_0}{2}\right)\sin^2\left(\frac{St_{swap}}{2}\right)} \tag{4.1.4}$$

where $N_{p,q,g/e}$ is the number of measurements in which the qubit is measured in state p and the probe in state q if the qubit was initially at state $|g\rangle/|e\rangle$,N_{SD} is the number of events in which unambigous state discrimination was possible. The noise in this case is given by:

$$\Delta\tilde{S} = \sqrt{\sum_{i=1,0}\sum_{j=e,g}\left(\frac{\partial\tilde{S}}{\partial N_{i,j}}\right)^2 \Delta N_{i,j}^2} \simeq \sqrt{N_{SD}} \cdot \frac{\sin\left(\frac{\theta_0}{2}\right)\cos\left(\frac{\theta_0}{2}\right)\sin\left(\frac{St_{swap}}{2}\right)}{\sin^2\left(\frac{\theta_0}{2}\right)+\cos^2\left(\frac{\theta_0}{2}\right)\sin^2\left(\frac{St_{swap}}{2}\right)} \tag{4.1.5}$$

for $\theta_0 \ll 1$ and the SNR for a state discrimination protocol is:

$$SNR_{SD}(N) = \frac{\tilde{S}}{\Delta\tilde{S}} \simeq \frac{V_{SD}\cdot\theta_0\sqrt{N\left[(St_{swap})^2+(\theta_0)^2\right]}}{\sqrt{2}St_{swap}} \tag{4.1.6}$$

SNR_{SD} thus increases with shorter swap time or weaker coupling strength. In the case of decoherence SNR_{SD} was calculated as follows: $\tilde{S} = V_{SD}N_{SD}\frac{\rho_{11}}{\rho_{10}+\rho_{11}}$; $\Delta\tilde{S} = \frac{\sqrt{N_{SD}\rho_{11}\rho_{10}}}{\rho_{10}+\rho_{11}}$. Fig. 4.2 shows the SNR ratio of the two protocols. In Fig. 4.2a the SNR ratio increases with $\sin^2\left(\frac{\theta_0}{2}\right)$ in a manner expected by the discrimination probability in the numerator. Decoherence tends to destroy the SNR amplification but only by a factor of ~ 2. The effect of decoherence is harsh when t_{swap} is decreased. As can be seen from Fig. 4.2b, although without decoherence the SNR ratio is increased by 1-2 orders of magnitude as t_{swap} decreases, decoherence poses a limit to the level of amplification, even for very short (~0.01 ns) swap time. Nevertheless, for the parameters of the phase qubit system, amplification by a factor of 2 is acheivable and can be in priniciple as large as 10 for a smaller coupling capacitor.

4.2 Pythagorean Coupling in a 4-Level Qudit

4.2.1 Pythagorean Coupling Theory

A theory for complete population transfer in a four level system has been formulated by Suchowski et al in 2011[83]. In the paper, population dynamics

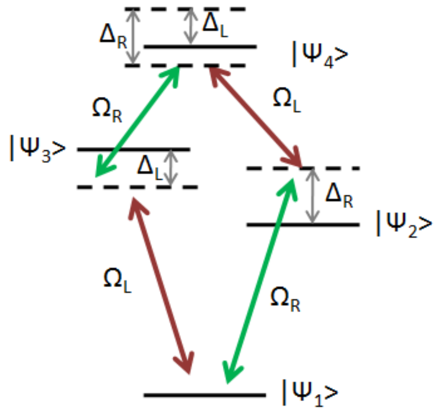

Fig. 4.3: Energy level diagram of 4-level qudit dynamics in the $SU(2) \bigotimes SU(2)$ representation including detuning of the drives.

were explored from a geometrical point of view. In a way similar to the Bloch sphere description of a two level state, using the isomorphism the orthonormal group SO(4) and two separate SU(2) groups, the evolution in a transformed basis named the Bell basis can be viewed geometrically on two different Bloch spheres (see Fig. 4.3). As seen in the figure, each sphere has its unique Rabi frequency and effective detuning corresponding to separate couplings between nearest neighbour states and next nearest neighbour states in the Bell basis, respectively. In systems with ladder-type coupling in which the coupling coefficient between level one and four is zero, it is shown that complete population transfer between level one and three occurs when the three coupling coefficients satisfy the pythagorean equation. The coefficients do not possess a common factor and are therefore primitive pythagorean triplets (PPT). While coherent manipulation of a qudit has been shown previously[5], the pythagorean condition was not explicitly demonstrated. In the next section simulation results with experimental parameters of current samples are shown that determine the feasibility of an experiment that tests the above predicitions.

4.2.2 Simulation

Simulations were done using the following Hamiltonian to model the superconducting 4-level qudit system with the drive using the rotating wave approximation (see Appendix B for details):

$$H = \begin{pmatrix} 0 & V & 0 & 0 \\ V* & 0 & \sqrt{2}\cdot V & 0 \\ 0 & \sqrt{2}\cdot V* & \Delta_1 & \sqrt{3}\cdot V \\ 0 & 0 & \sqrt{3}\cdot V* & \Delta_2 \end{pmatrix} \tag{4.2.1}$$

where $V = \frac{\hbar}{2}\left(\Omega c + \frac{\Omega a}{\sqrt{2}}e^{i\beta_1 t} + \frac{\Omega b}{\sqrt{3}}e^{i\beta_2 t}\right)$,$\frac{\Omega}{2\pi}$ is the Rabi frequency, $\beta_{1,2}$ is the level anharmonicity ($\omega_{21} - \omega_{10}$ and $\omega_{32} - \omega_{10}$ respectively) and $\Delta_{1,2}$ is the detuning $((\omega_{20} - 2\cdot\omega_{10}), (\omega_{30} - 3\cdot\omega_{10})$, respectively). $\{c, a, b\}$ are the PPT coefficients: $c = \frac{p^2+q^2}{2}, a = pq, b = \frac{p^2-q^2}{2}$.

There are two effects that have to be considered when simulating the experiment: first, small anharmonicity in the superconducting qubits $(\sim 200MHz)$ results in unwanted multiphoton excitations for sufficiently high Rabi amplitudes since the multi-photon absorption rate scales as $\frac{\Omega^2}{\beta}$[84]. Second, due to decay and decoherence the qubit manipulation has to be short enough. Since the population inversion time is inversely proportional to the Rabi amplitude, the last has to be larger to compensate for the short duration leading to more unwanted excitations. Thus, it is necessary to optimize the pulse length to be as long as possible for specific decay and dephasing times.

In the simulation, p and q were varied to form a density plot of the second excited state probability. Results are shown in Fig. 4.4. Fig 4.4a shows simulation results without decoherence, large anharmonicity and weak and relatively long $\tau_{exc} = 200$ ns excitation pulse. The simulation shows that in these ideal

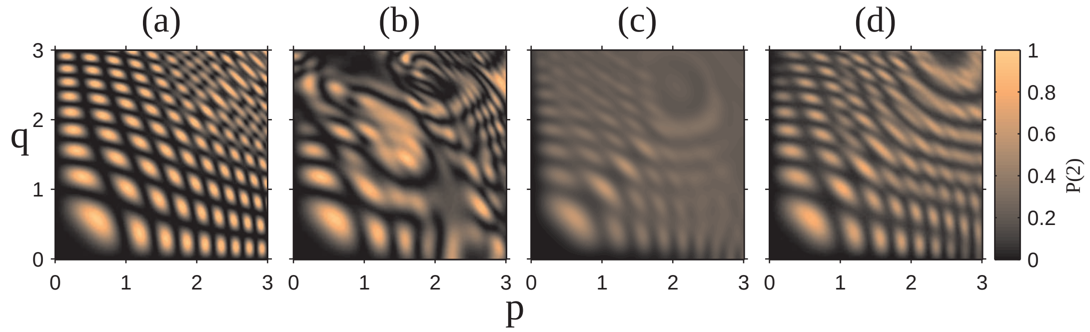

Fig. 4.4: Complete population transfer probability versus PPT generating numbers p and q. (a) The case of no decoherence and large anharmonicity $\beta_1 = \frac{\beta_2}{2} = 1$ GHz; τ_{exc} =200 ns; $\frac{\Omega}{2\pi} = 10$ MHz. (b) Phase qubit parameters without decoherence: $\beta_1 = \frac{\beta_2}{2} = 200$ MHz; τ_{exc} =40 ns; $\frac{\Omega}{2\pi} = 50$ MHz. (c) $T_1 = 300$ ns, $T_2 = 100$ ns; $\beta_1 = \frac{\beta_2}{2} = 200$ MHz;$\tau_{exc} = 80$ ns; $\frac{\Omega}{2\pi} = 25$ MHz. (d) Transmon parameters: $T_1 = 760$ ns, $T_2 = 920$ ns; $\beta_1 = \frac{\beta_2}{2} = 200$ MHz;τ_{exc} =120 ns; $\frac{\Omega}{2\pi} = 17$ MHz.

conditions, complete population transfer is demonstrated when p 3and q satisfy the PPT relation as expected. In Fig. 4.3b results are shown for a phase qubit without decoherence. While the first three triplets are visible, the multiphoton excitations have a significant effect on larger p, q due to the smaller anharmonicity and the higher rabi amplitude. Fig. 4.4c shows decoherence effects on the phase qubit. Excitation pulse is longer to reduce multiphoton effects. In this case more pythagorean triplets are seen, leading to the conclusion that multiphoton excitations have a larger effect than decoherence. Fig. 4.3d shows the results with longer decay and dephasing time corresponding to the transmon qubit. This allows τ_{exc} to be even longer leading to more visible triplets. To conclude, the pythagorean coupling experimental demonstration is feasible in both qubits and can be the subject of future experiments.

CHAPTER 5

Summary and Outlook

In this work we have introduced new methods of preparation and measurement of quantum states in superconducting qubits. A multidimensional genetic optimization of qubit excitation pulses was used to acheive single level states and superpositions with much higher fidelity than can be acheived manually. While demonstrated in the phase qubit, it can in principle be implemented in other systems such as the transmon qubit. This could be the basis of gate optimization in future work.

Using the above method, we have prepared and measured the Wigner distribution of Fock-state superpositions. The Wigner distribution was measured directly using the low anharmonicity that can be acheived in the phase qubit. The method was found to be calibration-free and can be used as an alternative, efficient method for state tomography. By extracting the density matrix from the Wigner distribution, it is possible to measure the decay and dephasing times of higher levels in an anharmonic system. This has only been demonstrated in harmonic systems[85]. Since the overhead in the number of measurements necessary to extract the density matrix from the Wigner distribution was found to be larger only by a factor of 8 relative to state tomography, it can be used in the genetic optimization to prepare states with a defined phase. Using the Wigner measurement, we have managed to observe phase-locking between the system and the drive.

A different part of this work was to set-up and measure a transmon qubit.

We were unsuccessful at measuring the qubit, probably because the coupling to the resonator was weak. Finally, we have shown two simulations for future experiments. The first one demonstrated state discrimination between a thermally excited state and the ground state that is important for future qubits with improved decay times in which thermal excitations are considerable. The method presented in this work can theoretically improve SNR over a direct measurement. The second simulation analyzed the possibility of experimentally measuring the effect of pythagorean coupling in four-level qudits. Both experiments were shown to be feasible in current samples and can be measured in future projects.

Bibliography

[1] Michael A. Nielsen and Isaac L. Chuang. *Quantum Computation and Quantum Information (Cambridge Series on Information and the Natural Sciences)*. Cambridge University Press, 2004.

[2] Seth Lloyd. Universal quantum simulators. *Science*, 273(5278):1073–1078, 1996.

[3] Ashok Muthukrishnan and C. R. Stroud. Multivalued logic gates for quantum computation. *Phys. Rev. A*, 62:052309, Oct 2000.

[4] Benjamin P. Lanyon, Marco Barbieri, Marcelo P. Almeida, Thomas Jennewein, Timothy C. Ralph, Kevin J. Resch, Geoff J. Pryde, Jeremy L. O'Brien, Alexei Gilchrist, and Andrew G. White. Simplifying quantum logic using higher-dimensional Hilbert spaces. *Nature Physics*, 5(2):134–140, December 2008.

[5] Matthew Neeley, Markus Ansmann, Radoslaw C. Bialczak, Max Hofheinz, Erik Lucero, Aaron D. O'Connell, Daniel Sank, Haohua Wang, James Wenner, Andrew N. Cleland, Michael R. Geller, and John M. Martinis. Emulation of a Quantum Spin with a Superconducting Phase Qudit. *Science*, 325(5941):722–725, August 2009.

[6] Dagomir Kaszlikowski, Piotr Gnaciński, Marek Żukowski, Wieslaw Miklaszewski, and Anton Zeilinger. Violations of local realism by two entangled N-dimensional systems are stronger than for two qubits. *Phys. Rev. Lett.*, 85:4418–4421, Nov 2000.

[7] Eric M. Rains. Nonbinary quantum codes. *IEEE Transactions on Information Theory*, 45(6):1827–1832, 1999.

[8] Weihs Gregor Zeilinger Anton Mair Alois, Vaziri Alipasha. Entanglement of the orbital angular momentum states of photons. *Nature*, 412:313–316, 2001.

[9] G. Molina-Terriza, A. Vaziri, J. Řeháček, Z. Hradil, and A. Zeilinger. Triggered qutrits for quantum communication protocols. *Phys. Rev. Lett.*, 92:167903, Apr 2004.

[10] Giuseppe Vallone, Enrico Pomarico, Francesco De Martini, Paolo Mataloni, and Marco Barbieri. Experimental realization of polarization qutrits from nonmaximally entangled states. *Phys. Rev. A*, 76:012319, Jul 2007.

[11] R. T. Thew, A. Acin, H. Zbinden, and N. Gisin. Bell-type test of energy-time entangled qutrits. *Phys. Rev. Lett.*, 93:010503, Jul 2004.

[12] R. Bianchetti, S. Filipp, M. Baur, J. M. Fink, C. Lang, L. Steffen, M. Boissonneault, A. Blais, and A. Wallraff. Control and tomography of a three level superconducting artificial atom. *Phys. Rev. Lett.*, 105:223601, Nov 2010.

[13] L. Allen and J. H. Eberly. *Optical Resonance and Two-Level Atoms*. Dover Publications, December 1987.

[14] W. Meissner and R. Ochsenfeld. Ein neuer effekt bei eintritt der supraleitfahigkeit. *Naturwissenschaften*, 21:787–788, 1933.

[15] F. London and H. London. The electromagnetic equations of the supraconductor. *Proceedings of the Royal Society of London. Series A - Mathematical and Physical Sciences*, 149(866):71–88, 1935.

[16] J. Bardeen, L. N. Cooper, and J. R. Schrieffer. Theory of superconductivity. *Phys. Rev.*, 108:1175–1204, Dec 1957.

[17] L.D. Landau. *Collected papers of L. D. Landau*. Gordon and Breach, 1965.

[18] B. D. Josephson. Possible new effects in superconductive tunnelling. *Physics Letters*, 1(7):251–253, July 1962.

[19] JOHN CLARKE, ANDREW N. CLELAND, MICHEL H. DEVORET, DANIEL ESTEVE, and JOHN M. MARTINIS. Quantum mechanics of a macroscopic variable: The phase difference of a josephson junction. *Science*, 239(4843):992–997, 1988.

[20] Michel H. Devoret, John M. Martinis, and John Clarke. Measurements of macroscopic quantum tunneling out of the zero-voltage state of a current-biased josephson junction. *Phys. Rev. Lett.*, 55:1908–1911, Oct 1985.

[21] M. H. Devoret. *Quantum Fluctuations*. Les Houches Session LXIII, 1995.

[22] John M. Martinis, S. Nam, J. Aumentado, and C. Urbina. Rabi oscillations in a large josephson-junction qubit. *Phys. Rev. Lett.*, 89(11):117901, Aug 2002.

[23] Markus Ansmann, H. Wang, Radoslaw C. Bialczak, Max Hofheinz, Erik Lucero, M. Neeley, A. D. O'Connell, D. Sank, M. Weides, J. Wenner, A. N. Cleland, and John M. Martinis. Violation of Bell's inequality in Josephson phase qubits. *Nature*, 461(7263):504–506, September 2009.

[24] Matthias Steffen, M. Ansmann, Radoslaw C. Bialczak, N. Katz, Erik Lucero, R. McDermott, Matthew Neeley, E. M. Weig, A. N. Cleland, and John M. Martinis. Measurement of the Entanglement of Two Superconducting Qubits via State Tomography. *Science*, 313(5792):1423–1425, September 2006.

[25] L. DiCarlo, M. D. Reed, L. Sun, B. R. Johnson, J. M. Chow, J. M. Gambetta, L. Frunzio, S. M. Girvin, M. H. Devoret, and R. J. Schoelkopf. Preparation and measurement of three-qubit entanglement in a superconducting circuit. *Nature*, 467(7315):574–578, September 2010.

[26] W. C. Stewart. Current-voltage characteristics of josephson junctions. *Applied Physics Letters*, 12(8):277–280, 1968.

[27] D. E. McCumber. Effect of ac impedance on dc voltage-current characteristics of superconductor weak-link junctions. *Journal of Applied Physics*, 39(7):3113–3118, 1968.

[28] John M. Martinis, Michel H. Devoret, and John Clarke. Energy-level quantization in the zero-voltage state of a current-biased josephson junction. *Phys. Rev. Lett.*, 55(15):1543–1546, Oct 1985.

[29] R. W. Simmonds, K. M. Lang, D. A. Hite, S. Nam, D. P. Pappas, and John M. Martinis. Decoherence in josephson phase qubits from junction resonators. *Phys. Rev. Lett.*, 93(7):077003, Aug 2004.

[30] J. Clarke and A.I. Braginski. *The SQUID Handbook: Fundamentals and Technology of SQUIDs and SQUID Systems*. Number v. 1. Wiley, 2006.

[31] A. Barone and G. Paterno. *Physics and applications of the Josephson effect*. UMI Out-of-Print Books on Demand. Wiley, 1982.

[32] V Bouchiat, D Vion, P Joyez, D Esteve, and M H Devoret. Quantum coherence with a single cooper pair. *Physica Scripta*, 1998(T76):165, 1998.

[33] Jens Koch, Terri M. Yu, Jay Gambetta, A. A. Houck, D. I. Schuster, J. Majer, Alexandre Blais, M. H. Devoret, S. M. Girvin, and R. J. Schoelkopf.

Charge-insensitive qubit design derived from the cooper pair box. *Phys. Rev. A*, 76:042319, Oct 2007.

[34] Alexandre Blais, Ren-Shou Huang, Andreas Wallraff, S. M. Girvin, and R. J. Schoelkopf. Cavity quantum electrodynamics for superconducting electrical circuits: An architecture for quantum computation. *Phys. Rev. A*, 69:062320, Jun 2004.

[35] David Isaac Schuster. *Cavity Quantum Electrodynamics*. PhD thesis, Yale University, 2007.

[36] John M. Martinis, K. B. Cooper, R. McDermott, Matthias Steffen, Markus Ansmann, K. D. Osborn, K. Cicak, Seongshik Oh, D. P. Pappas, R. W. Simmonds, and Clare C. Yu. Decoherence in josephson qubits from dielectric loss. *Phys. Rev. Lett.*, 95(21):210503, Nov 2005.

[37] Martin P. Weides, Jeffrey S. Kline, Michael R. Vissers, Martin O. Sandberg, David S. Wisbey, Blake R. Johnson, Thomas A. Ohki, and David P. Pappas. Coherence in a transmon qubit with epitaxial tunnel junctions. *Applied Physics Letters*, 99(26):262502, 2011.

[38] Jeffrey S Kline, Michael R Vissers, Fabio C S da Silva, David S Wisbey, Martin Weides, Terence J Weir, Benjamin Turek, Danielle A Braje, William D Oliver, Yoni Shalibo, Nadav Katz, Blake R Johnson, Thomas A Ohki, and David P Pappas. Sub-micrometer epitaxial josephson junctions for quantum circuits. *Superconductor Science and Technology*, 25(2):025005, 2012.

[39] G.C. Tettamanzi, C.I. Pakes, A. Potenza, C.H. Marrows, S. Prawer, and D.N. Jamieson. Superconducting microbridge junctions fabricated using

focused ion beams. In *Nanoscience and Nanotechnology, 2006. ICONN '06. International Conference on*, july 2006.

[40] Tom Ohki Jiansong Gao Jose Aumentado Martin Weides David P. Pappas Martin O. Sandberg, Michael R. Vissers. Long-lived, radiation-suppressed superconducting quantum bit in a planar geometry. *arXiv:1211.2017v1*, 2012.

[41] M. D. Shaw, R. M. Lutchyn, P. Delsing, and P. M. Echternach. Kinetics of nonequilibrium quasiparticle tunneling in superconducting charge qubits. *Phys. Rev. B*, 78:024503, Jul 2008.

[42] John M. Martinis, M. Ansmann, and J. Aumentado. Energy decay in superconducting josephson-junction qubits from nonequilibrium quasiparticle excitations. *Phys. Rev. Lett.*, 103:097002, Aug 2009.

[43] Matthew Neeley, M. Ansmann, Radoslaw C. Bialczak, M. Hofheinz, N. Katz, Erik Lucero, A. O'Connell, H. Wang, A. N. Cleland, and John M. Martinis. Transformed dissipation in superconducting quantum circuits. *Physical Review B (Condensed Matter and Materials Physics)*, 77(18):180508, 2008.

[44] E. M. Purcell. Spontaneous emission probabilities at radio frequencies. *Physical Review*, 69:681, 1946.

[45] A. A. Houck, J. A. Schreier, B. R. Johnson, J. M. Chow, Jens Koch, J. M. Gambetta, D. I. Schuster, L. Frunzio, M. H. Devoret, S. M. Girvin, and R. J. Schoelkopf. Controlling the spontaneous emission of a superconducting transmon qubit. *Phys. Rev. Lett.*, 101:080502, Aug 2008.

[46] John M. Martinis, S. Nam, J. Aumentado, K. M. Lang, and C. Urbina.

Decoherence of a superconducting qubit due to bias noise. *Phys. Rev. B*, 67:094510, Mar 2003.

[47] Radoslaw C. Bialczak, R. McDermott, M. Ansmann, M. Hofheinz, N. Katz, Erik Lucero, Matthew Neeley, A. D. O'Connell, H. Wang, A. N. Cleland, and John M. Martinis. $1/f$ flux noise in josephson phase qubits. *Phys. Rev. Lett.*, 99:187006, Nov 2007.

[48] Frederick C. Wellstood, Cristian Urbina, and John Clarke. Low-frequency noise in dc superconducting quantum interference devices below 1 k. *Applied Physics Letters*, 50(12):772–774, 1987.

[49] S. Sendelbach, D. Hover, A. Kittel, M. Muck, John M. Martinis, and R. McDermott. Magnetism in squids at millikelvin temperatures. *Physical Review Letters*, 100(22):227006, 2008.

[50] Jiansheng Wu and Clare C. Yu. Modeling flux noise in squids due to hyperfine interactions. *Phys. Rev. Lett.*, 108:247001, Jun 2012.

[51] Yoni Shalibo, Ya'ara Rofe, David Shwa, Felix Zeides, Matthew Neeley, John M. Martinis, and Nadav Katz. Lifetime and coherence of two-level defects in a josephson junction. *Phys. Rev. Lett.*, 105(17):177001, Oct 2010.

[52] F. Pobell. *Matter and Methods at Low Temperatures*. Springer-Verlag, 1996.

[53] G. Frossati. Experimental techniques: Methods for cooling below 300 mk. *Journal of Low Temperature Physics*, 87, Issue 3-4:595–633, 1992.

[54] R. Radebaugh and J.D. Siegwarth. Dilution refrigerator technology. *Cryogenics*, 11(5):368 – 384, 1971.

[55] A.T.A.M. Waele. Basic operation of cryocoolers and related thermal machines. *Journal of Low Temperature Physics*, 164:179–236, 2011.

[56] A.T.A.M. de Waele, P.P. Steijaert, and J. Gijzen. Thermodynamical aspects of pulse tubes. *Cryogenics*, 37(6):313 – 324, 1997.

[57] Ya'ara Rofe. Transition from ladder climbing to autoresonance in the flux bias josephson phase circuits. Master's thesis, Hebrew University of Jerusalem, 2010.

[58] Martinis Group. Josephson junction quantum computing at ucsb. http://web.physics.ucsb.edu/∼martinisgroup/.

[59] Yoni Shalibo. *Control and measurement of multi-level states in the Josephson phase qubit*. PhD thesis, Hebrew University of Jerusalem, 2012.

[60] J. M. Schmidt, A. N. Cleland, and John Clarke. Resonant tunneling in small current-biased josephson junctions. *Phys. Rev. B*, 43:229–238, Jan 1991.

[61] Erik Lucero, M. Hofheinz, M. Ansmann, Radoslaw C. Bialczak, N. Katz, Matthew Neeley, A. D. O'Connell, H. Wang, A. N. Cleland, and John M. Martinis. High-fidelity gates in a single josephson qubit. *Phys. Rev. Lett.*, 100(24):247001, Jun 2008.

[62] Jay Gambetta, Alexandre Blais, D. I. Schuster, A. Wallraff, L. Frunzio, J. Majer, M. H. Devoret, S. M. Girvin, and R. J. Schoelkopf. Qubit-photon interactions in a cavity: Measurement-induced dephasing and number splitting. *Phys. Rev. A*, 74:042318, Oct 2006.

[63] J.H. Holland. *Adaptation in natural and artificial systems: an introductory analysis with applications to biology, control, and artificial intelligence*. University of Michigan Press, 1975.

[64] Hod Lipson and Jordan B. Pollack. Automatic design and manufacture of robotic lifeforms. *Nature*, 406:974–978, 2000.

[65] Michael Schmidt and Hod Lipson. Distilling free-form natural laws from experimental data. *Science*, 324(5923):81–85, 2009.

[66] O. J. Mengshoel and D. E. Goldberg. The crowding approach to niching in genetic algorithms. *Evolutionary Computation*, 16(3):315–354, 2008.

[67] E. Wigner. On the quantum correction for thermodynamic equilibrium. *Phys. Rev.*, 40:749–759, Jun 1932.

[68] Matthias Steffen, M. Ansmann, R. McDermott, N. Katz, Radoslaw C. Bialczak, Erik Lucero, Matthew Neeley, E. M. Weig, A. N. Cleland, and John M. Martinis. State tomography of capacitively shunted phase qubits with high fidelity. *Physical Review Letters*, 97(5):050502, 2006.

[69] P. Bertet, A. Auffeves, P. Maioli, S. Osnaghi, T. Meunier, M. Brune, J. M. Raimond, and S. Haroche. Direct measurement of the wigner function of a one-photon fock state in a cavity. *Phys. Rev. Lett.*, 89:200402, Oct 2002.

[70] C. Eichler, D. Bozyigit, C. Lang, L. Steffen, J. Fink, and A. Wallraff. Experimental state tomography of itinerant single microwave photons. *Phys. Rev. Lett.*, 106:220503, Jun 2011.

[71] T. J. Dunn, I. A. Walmsley, and S. Mukamel. Experimental determination of the quantum-mechanical state of a molecular vibrational mode using fluorescence tomography. *Phys. Rev. Lett.*, 74:884–887, Feb 1995.

[72] Antoine Royer. Wigner function as the expectation value of a parity operator. *Phys. Rev. A*, 15:449–450, Feb 1977.

[73] Max Hofheinz, H. Wang, M. Ansmann, Radoslaw C. Bialczak, Erik Lucero, M. Neeley, A. D. O'Connell, D. Sank, J. Wenner, John M. Martinis, and A. N. Cleland. Synthesizing arbitrary quantum states in a superconducting resonator. *Nature*, 459(7246):546–549, May 2009.

[74] J. Fajans and L. Friedland. Autoresonant (nonstationary) excitation of pendulums, plutinos, plasmas, and other nonlinear oscillators. *American Journal of Physics*, 69(10):1096–1102, 2001.

[75] Yoni Shalibo, Ya'ara Rofe, Ido Barth, Lazar Friedland, Radoslaw Bialczack, John M. Martinis, and Nadav Katz. Quantum and classical chirps in an anharmonic oscillator. *Phys. Rev. Lett.*, 108:037701, Jan 2012.

[76] Wolfgang P. Schleich. *Quantum Optics in Phase Space*. Wiley-VCH, 1 edition, February 2001.

[77] Wilhelm Magnus. On the exponential solution of differential equations for a linear operator. *Communications on Pure and Applied Mathematics*, 7(4):649–673, 1954.

[78] I.D. Ivanovic. How to differentiate between non-orthogonal states. *Physics Letters A*, 123(6):257 – 259, 1987.

[79] Asher Peres. How to differentiate between non-orthogonal states. *Physics Letters A*, 128(1,2):19 –, 1988.

[80] B. Huttner, A. Muller, J. D. Gautier, H. Zbinden, and N. Gisin. Unambiguous quantum measurement of nonorthogonal states. *Phys. Rev. A*, 54:3783–3789, Nov 1996.

[81] Roger B. M. Clarke, Anthony Chefles, Stephen M. Barnett, and Erling Riis.

Experimental demonstration of optimal unambiguous state discrimination. *Phys. Rev. A*, 63:040305, Mar 2001.

[82] David J. Starling Gregory A. Howland John C. Howell Yuval Gefen Oded Zilberberg, Alessandro Romito. Null weak values and quantum state discrimination. *arXiv:1205.3877v1*, 2012.

[83] Haim Suchowski, Yaron Silberberg, and Dmitry B. Uskov. Pythagorean coupling: Complete population transfer in a four-state system. *Phys. Rev. A*, 84:013414, Jul 2011.

[84] Robert W. Boyd. *Nonlinear Optics, Third Edition*. Academic Press, 3rd edition, 2008.

[85] H. Wang, M. Hofheinz, M. Ansmann, R. C. Bialczak, Erik Lucero, M. Neeley, A. D. O'Connell, D. Sank, M. Weides, J. Wenner, A. N. Cleland, and John M. Martinis. Decoherence dynamics of complex photon states in a superconducting circuit. *Phys. Rev. Lett.*, 103(20):200404, Nov 2009.

[86] D. F. Walls and G. J. Milburn. Effect of dissipation on quantum coherence. *Phys. Rev. A*, 31:2403–2408, Apr 1985.

APPENDIX A

Pulse Calibration

A continuous function $f\,(t)$ sent to the DAC from the computer is sampled at time intervals $\Delta = 1$ ns and is defined as $f_n = f(n\Delta)$. The output of the DAC is given by:

$$g(t) = \sum_n f_n h(t - n\Delta) \tag{A.1}$$

where $h(t)$ is the response function of the DAC chain which is typically a 1.6 ns FWHM gaussian due to the gaussian filters at its outputs (see Sec. 2.2) with an induced ringing from reflections that are a result of impedance mismatch at the I and Q pathways (Fig. A.1).

By introducing the Dirac comb $Ш_\Delta(t) = \sum_{-\infty}^{\infty} \delta(t - n\Delta)$, $g(t)$ can be expressed as a function of $f(t)$:

$$g(t) = \int \sum_n f_n \delta(\tau - n\Delta) h(t - \tau) d\tau = \left[(f \cdot Ш_\Delta) * h \right](t) \tag{A.2}$$

$g(t)$ is thus a convolution of the input function $f(t)$ with the response function $h(t)$. While the DAC output $g(t)$ is typically not the desired pulse, it can be corrected by engineering the function $f(t)$ so that the output will be as planned. This is done by computing a function $f'(t)$ that is inserted to the DAC with the actual response function h_a that yields the function of the original $f(t)$ with the ideal response function that has no ringing h_i . This is expressed mathemati-

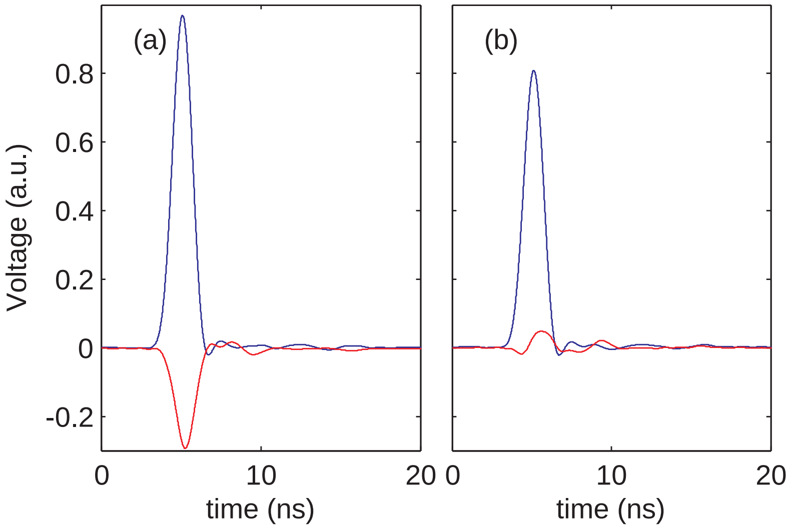

Fig. A.1: Impulse response of the DAC before correction. (a) Envelope of the measured signal when a 1 ns pulse is inserted to the I channel and (b) when inserted in the Q channel. The I component is shown in blue and Q in red.

cally as:

$$(f'\cdot) * h_a = (f \cdot \text{Ш}_\Delta) * h_i \tag{A.3}$$

The fourier transform of the equation is:

$$(\tilde{f}'*) \cdot \tilde{h}_a = (\tilde{f} * \tilde{\text{Ш}}_\Delta) \cdot \tilde{h}_i \tag{A.4}$$

where $\tilde{\text{Ш}}_\Delta(\nu) = \frac{1}{\Delta} \sum\limits_{n=-\infty}^{\infty} \delta(\nu - \frac{n}{\Delta})$. Due to the finite resolution of the DAC signal errors with frequencies higher than $\frac{1}{2\Delta}$ cannot be corrected. Consequently, all modes above $\frac{1}{2\Delta}$ are truncated in $\tilde{f}$,$\tilde{h}_i$, $\tilde{h}_a$, hence limiting the correction to 1 ns resolution. After truncation, the Dirac comb can be removed from Eq. A.4 and $\tilde{f}'$ is computed by:

$$\tilde{f}' = \tilde{f} \cdot \frac{\tilde{h}_i}{\tilde{h}_a} \tag{A.5}$$

Eq. A.5 is only valid for single channel correction. However, as shown ion Fig. A.1 and mentioned in Sec. 2.2, there is a crosstalk between the two channels in the IQ mixer which effectively mixes between channels I and Q. To correct that the above derivation is generalized as follows: without crosstalk, the computed functions are given by the linear equation:

$$\begin{pmatrix} \tilde{h}_{I_a} & 0 \\ 0 & \tilde{h}_{Q_a} \end{pmatrix} \begin{pmatrix} \tilde{I}' \\ \tilde{Q}' \end{pmatrix} = \begin{pmatrix} \tilde{h}_{I_i} & 0 \\ 0 & \tilde{h}_{Q_i} \end{pmatrix} \begin{pmatrix} \tilde{I} \\ \tilde{Q} \end{pmatrix} \tag{A.6}$$

where $\tilde{I}$ and $\tilde{Q}$ are the fourier transforms of the DAC input functions for channel I and Q, respectively. A crosstalk between the two channels is represented by the off-diagonal elements in the matrix on the left:

$$\begin{pmatrix} \tilde{h}_{II_a} & \tilde{h}_{IQ_a} \\ \tilde{h}_{QI_a} & \tilde{h}_{QQ_a} \end{pmatrix} \begin{pmatrix} \tilde{I}' \\ \tilde{Q}' \end{pmatrix} = \begin{pmatrix} \tilde{h}_{I_i} \tilde{I} \\ \tilde{h}_{Q_i} \tilde{Q} \end{pmatrix} \tag{A.7}$$

$\tilde{h}_{IQ_a}$ is the response function in the Q channel when a 1 ns pulse is given in the I channel and vice versa. Mutliplying both sides by the inverse of the response matrix gives:

$$\begin{pmatrix} \tilde{I}' \\ \tilde{y}' \end{pmatrix} = \frac{1}{\left(\tilde{h}_{II_a}\tilde{h}_{QQ_a} - \tilde{h}_{IQ_a}\tilde{h}_{QI_a}\right)} \begin{pmatrix} \tilde{h}_{QQ_a} & -\tilde{h}_{IQ_a} \\ -\tilde{h}_{QI_a} & \tilde{h}_{II_a} \end{pmatrix} \begin{pmatrix} \tilde{h}_{I_i} \tilde{I} \\ \tilde{h}_{Q_i} \tilde{Q} \end{pmatrix} \tag{A.8}$$

I' and Q' are computed using the inverse fourier transform of Eq. A.8. The correction is limited by the bandwidth of the DAC (~300 MHz). The correction reduces the ringing amplitude to 1% of the peak amplitude. The response is LO frequency dependant and thus the calibration is done for intervals of 10 MHz which is sufficient to ensure an accurate calibration.

Appendix B

Simulation Method

Simulations were done based on the phase qubit Hamiltonian (Eq. 1.3.8) with an added term: $I_d(t)\Phi_0\hat{\varphi}/2\pi$ where $I_d(t) = I(t)\cos(\omega t) + Q(t)\sin(\omega t)$ is the microwave drive. When the phase is localised in a potential well, the untrapped states in other wells can be ignored. When the anharmonicity is sufficently low, $\beta/\omega_{01} = 0.002 - 0.02$, the off-diagonal terms are close to those of the harmonic oscillator and the second and third off-diagonal terms in the Hamiltonian are two and three orders of magnitude lower than the first off-diagonal and are therfore ignored in the simulation. In order to eliminate fast oscillating terms to speed up computation the RWA (Sec. 1.2) was generalised to multi-level states. This was done by a drive-oriented transformation of the Hamiltonian (full derivation can be found in [59], appendix A) and discarding terms which oscillate at 2ω. Consequently, the multi-level Hamiltonian in the RWA is given by:

$$H_{\mathrm{N}}^{\mathrm{RWA}} = \hbar \begin{pmatrix} 0 & \Omega/2 & 0 & \cdots & 0 \\ \Omega^*/2 & -\Delta & \sqrt{2}\Omega/2 & 0 & \vdots \\ 0 & \sqrt{2}\Omega^*/2 & \beta_2 - 2\Delta & \sqrt{3}\Omega/2 & 0 \\ \vdots & 0 & \sqrt{3}\Omega^*/2 & \ddots & \sqrt{\mathrm{N}-1}\Omega/2 \\ 0 & \cdots & 0 & \sqrt{\mathrm{N}-1}\Omega^*/2 & \beta_{\mathrm{N}-1} - (\mathrm{N}-1)\Delta \end{pmatrix} \tag{B.1}$$

where $\Omega\left(t\right)=\frac{A(t)\Phi_{ext}\delta_{01}}{2\pi\hbar}e^{i\phi(t)}$ is the time dependant Rabi amplitude, $A\left(t\right)=\sqrt{I\left(t\right)^{2}+Q\left(t\right)^{2}}$, $\phi(t)=\arctan\left(Q(t)/I(t)\right)$ are the amplitude and phase of the drive, respectively, $\Delta=\omega-\omega_{01}$ is the detuning from the drive and $\beta_{n}=\omega_{n}-n\omega t$ are the cummulative anharmonicites.

Decoherence was implemented in the simulation using quantum operations [1]. The simulation was divided into small time steps compared to the timescales of changes in the rotating frame. In each step, the density matrix was propagated by: $\rho\left(t+\Delta t\right)=U^{\dagger}\left(t+\Delta t,t\right)\rho\left(t\right)U\left(t+\Delta t,t\right)$ where $U\left(t+dt,t\right)=\exp\left(-iH_{\mathrm{N}}^{\mathrm{RWA}}\Delta t/\hbar\right)$ and then operated on by Kraus operators to apply energy decay and decoherence. Energy decay was simulated by modeling the system and environment as coupled harmonic oscillators described by the Hamiltonian: $H_{ED}=\chi\left(a^{\dagger}b+b^{\dagger}a\right)$ where $\chi=1/T_{1}$. In this case the kraus operators are given by[1] :

$$E_{k}=\sum_{n}\sqrt{\left(\begin{array}{c}n\\k\end{array}\right)}\sqrt{\left(1-\gamma\right)^{n-k}\gamma^{k}}\left|k\right\rangle\left\langle n\right| \tag{B.2}$$

where $\gamma=1-e^{-\chi\Delta t}$. When these operators are applied on the level $|n\rangle$ it decays exponentially at a rate n/T_{1} as expected for harmonic oscillators in which interaction strength scales with level number and the coherence represented by the off-diagonal elements in the density matrix $\rho_{m,n}$ decay at a rate $\frac{m+n}{2T_{1}}$.

Modeling decoherence is done by the following Hamiltonian: $H_{PD}=\nu a^{\dagger}a(b+b^{\dagger})$, where $\nu=\sqrt{2\frac{\Delta t}{T_{2}}}$. The Kraus operators for decoherence are given by[1]:

$$E_{k}=\sum_{n}\frac{\left(\left(-i\nu\Delta t\right)a^{\dagger}a\right)^{2n-k}}{(n-k)!\sqrt{k!n!}}e^{\left(\left(\nu\Delta t\right)a^{\dagger}a\right)^{2}/2} \tag{B.3}$$

When applied they induce a decay of $\rho_{n,m}$ at a rate $\frac{(m+n)^{2}}{T_{2}}$, in agreement with

---

[1] Derivation is not presented here but is available in a private write-up by Roy Resh and Yoni Shalibo

[86]. These models were found to be consistent with measurements on superconducting resonators[85].